JACS JOURNAL OF THE AMERICAN CHEMICAL SOCIETY

Article

Cite This: J. Am. Chem. Soc. 2019, 141, 16706−16725

pubs.acs.org/JACS

Ionic and Electronic Conduction in $TiNb_2O_7$

Kent J. Griffith,[†,#] Ieuan D. Seymour,[†,∥,#] Michael A. Hope,[†] Megan M. Butala,[‡] Leo K. Lamontagne,[‡] Molleigh B. Preefer,[‡] Can P. Koçer,[§] Graeme Henkelman,[∥] Andrew J. Morris,[⊥] Matthew J. Cliffe,[†,▽] Siân E. Dutton,[§] and Clare P. Grey*[,†]

[†]Department of Chemistry, University of Cambridge, Cambridge CB2 1EW, United Kingdom

[‡]Materials Department and Materials Research Laboratory, University of California, Santa Barbara, California 93106, United States of America

[§]Cavendish Laboratory, University of Cambridge, Cambridge CB3 0HE, United Kingdom

[∥]Department of Chemistry and the Oden Institute for Computational Engineering and Sciences, The University of Texas at Austin, Austin, Texas 78712, United States

[⊥]School of Metallurgy and Materials, University of Birmingham, Edgbaston, Birmingham B15 2TT, United Kingdom

[▽]School of Chemistry, University of Nottingham, University Park, Nottingham NG7 2RD, United Kingdom

Supporting Information

ABSTRACT: $TiNb_2O_7$ is a Wadsley−Roth phase with a crystallographic shear structure and is a promising candidate for high-rate lithium ion energy storage. The fundamental aspects of the lithium insertion mechanism and conduction in $TiNb_2O_7$, however, are not well-characterized. Herein, experimental and computational insights are combined to understand the inherent properties of bulk $TiNb_2O_7$. The results show an increase in electronic conductivity of seven orders of magnitude upon lithiation and indicate that electrons exhibit both localized and delocalized character, with a maximum Curie constant and Li NMR paramagnetic shift near a composition of $Li_{0.60}TiNb_2O_7$. Square-planar or distorted-five-coordinate lithium sites are calculated to invert between thermodynamic minima or transition states. Lithium diffusion in the single-redox region (i.e., $x \leq 3$ in $Li_xTiNb_2O_7$) is rapid with low activation barriers from NMR and $D_{Li} = 10^{-11}$ m^2 s^{-1} at the temperature of the observed T_1 minima of 525−650 K for $x \geq 0.75$. DFT calculations predict that ionic diffusion, like electronic conduction, is anisotropic with activation barriers for lithium hopping of 100−200 meV down the tunnels but ca. 700−1000 meV across the blocks. Lithium mobility is hindered in the multiredox region (i.e., $x > 3$ in $Li_xTiNb_2O_7$), related to a transition from interstitial-mediated to vacancy-mediated diffusion. Overall, lithium insertion leads to effective n-type self-doping of $TiNb_2O_7$ and high-rate conduction, while ionic motion is eventually hindered at high lithiation. Transition-state searching with beyond Li chemistries (Na^+, K^+, Mg^{2+}) in $TiNb_2O_7$ reveals high diffusion barriers of 1−3 eV, indicating that this structure is specifically suited to Li^+ mobility.

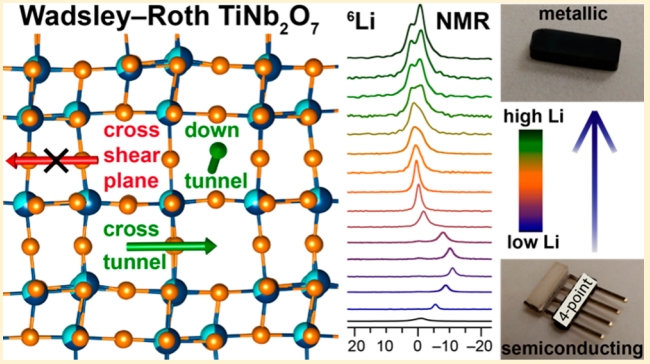

INTRODUCTION

Next-generation energy storage materials with fast recharging and high power capability are of immediate interest to accelerate widespread electric vehicle adoption.[1] Improved high-rate and high-capacity energy storage performance would also enable quick-charging portable devices and power-intensive tools, as well as not yet feasible applications that require power higher than that of conventional batteries and charge storage greater than that of supercapacitors. For negative electrodes (anodes) in rechargeable lithium ion batteries, graphite and other materials (e.g., silicon) that store a large quantity of lithium in a potential range close to the Li^+/Li redox couple are favored for high-energy density applications. However, large overpotentials and spatial overpotential inhomogeneities at high current densities can lead to lithium plating on the surface of low-voltage electrodes.[2−6] When lithium deposits as mossy or dendritic structures[7−10]—rather than plating smoothly onto a Li anode—the cell can short-circuit and undergo rapid heating that may lead to a battery fire/explosion.[11−14]

In order to overcome the inherent challenges associated with the use of low-voltage electrode materials in high-rate applications, a series of higher-voltage anode material candidates are emerging. Lithium titanate spinel, $Li_4Ti_5O_{12}$, is the most established of these with an average voltage of 1.55 V vs Li^+/Li and an accessible capacity of about 150 mA h g^{-1}, while other candidates include bronze-related TiO_2(B),[15−18]

Received: June 24, 2019
Published: September 5, 2019

T-Nb_2O_5,[19−22] $Nb_{18}W_{16}O_{93}$,[23] and crystallographic shear (cs) structures such as $Nb_{16}W_5O_{55}$[23] and $TiNb_2O_7$.[24−31] An average lithiation potential of ca. 1.5 V lowers the energy density at the full cell level in comparison to the standard graphite anode at ca. 0.1 V; however, high-voltage oxide anodes preclude dendrite formation even under very high current density lithiation, limit SEI formation, do not suffer the degradation of graphite at high rates, and can still offer reasonable cell energy with high density atomic structures and particle morphologies.

Crystallographically, $TiNb_2O_7$ belongs to a family of compounds known as Wadsley−Roth phases: block phases exhibiting crystallographic shear planes at the borders of ReO_3-like regions (blocks) of corner-shared octahedra. $TiNb_2O_7$ (Figure 1) comprises blocks that are three octahedra wide and

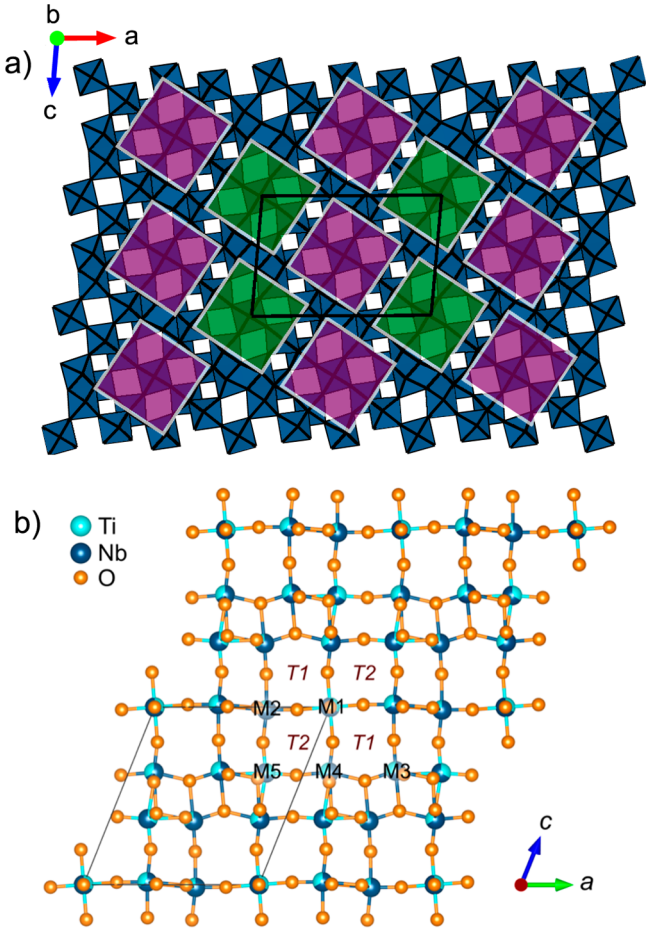

Figure 1. Crystal structure of the Wadsley−Roth phase $TiNb_2O_7$. (a) The $(3 \times 3)_\infty$ blocks of ReO_3-like octahedra are shaded; purple and green shaded blocks are offset by 1/2*b* in the structure. (b) Thirty-atom unit cell structure of $TiNb_2O_7$ used in DFT calculations. The five symmetrically distinct transition-metal (M) sites are labeled M_1−M_5, following the nomenclature of Perfler et al.[1] The two types of infinite tunnels along the *b* axis are labeled T1 and T2.

three octahedra long, and the blocks are infinitely connected in each plane (as opposed to blocks separated by tetrahedra in e.g. $TiNb_{24}O_{62}$ or the niobium tungsten oxides); this motif is denoted $(3 \times 3)_\infty$. $TiNb_2O_7$, the most titanium-rich ternary member of the mixed TiO_2−Nb_2O_5 series,[32,33] has demonstrated promise for its high rate capability in various nanostructures and its high theoretical capacity. A capacity of 232.7 mA h g^{-1} would be expected on the basis of one-electron reductions of Ti^{4+} to Ti^{3+} and Nb^{5+} to Nb^{4+} (i.e., $Li_3TiNb_2O_7$), with additional capacity reported through multielectron redox or "overlithiation" beyond one lithium per transition metal (Li/TM). Previous studies have focused on aspects of the structural mechanism of lithiation in $TiNb_2O_7$[34,28,35] and performance-optimizing synthetic strategies.[26−28,30,36−41] In addition to the generic challenges associated with implementing nanostructured particles for energy storage—cost, stability, and scalability[42]—$TiNb_2O_7$ also specifically exhibits problematic gas evolution that is exacerbated by high-surface-area morphologies.[41] In this work, we approach the fundamental aspects of electrochemical energy storage in $TiNb_2O_7$ by studying the lithiation of low-surface-area, micrometer-scale particles. A combined experimental and computational quantitative analysis is performed to understand the lithium and electron transport properties that enable high-rate performance in large particles of this wide-band-gap oxide. This has implications for many other insulating early-transition-metal oxide electrode candidates with d^0 electron configurations.

Solid-state nuclear magnetic resonance (NMR) spectroscopy is a versatile probe of local atomic and electronic structure, as well as ion dynamics, that has been widely applied to study transport and failure mechanisms in electrochemical energy storage materials.[43,44] As NMR spectra are sensitive to localized paramagnetism and delocalized Pauli paramagnetic effects (known as Knight shifts) as well as diamagnetic shielding from local coordination environments, we follow the changes that lithium insertion induces in the electronic and magnetic properties of $TiNb_2O_7$.

Nuclear magnetic relaxation is mediated by fluctuations on the time scale of the nuclear Larmor frequency (ω_0). Thus, when diffusion modulates the NMR couplings (e.g., dipolar, quadrupolar, and/or hyperfine), T_1 relaxation serves as a probe of atomic motion.[45−47] The time variation of the ^{7}Li *z* magnetization can be derived from the spectral density function of the motion, $J(\omega)$. Assuming that the correlation function for the diffusional motion is monoexponential, it is possible to compute the spectral density; this is the basis of the well-established Bloembergen−Purcell−Pound (BPP) model for analyzing relaxation due to atomic motion.[48] Here, the ^{7}Li NMR relaxation in $Li_xTiNb_2O_7$ is examined over a wide temperature range, ca. 300−1000 K, and motional activation energies are extracted as a function of lithiation, i.e. state of charge. In favorable cases, where a T_1 minimum can be identified, it is possible to extract the lithium diffusivity via the Einstein−Smoluchowski relation. These NMR results are correlated with complementary analyses including magnetic susceptibility, electronic conductivity, and multipurpose density functional theory (DFT) calculations.

Ab initio calculations complement the experimental results by evaluating the cation configurations and predicting diffusion pathways and energy barriers, as well as the local environments. First of all, calculations on the host $TiNb_2O_7$ crystallographic shear structure set the scene for further calculations of lithium kinetics and spectroscopic signatures. Due to the mixed occupancy of Ti and Nb on the five crystallographically-distinct octahedral metal sites in $TiNb_2O_7$, cation configurations were enumerated and their energies minimized and thermodynamically ranked. Once lithium ions were added, a single-ended transition state searching method based on hybrid eigenvector following (HEF) was used in this work to explore minima and transition states on the complex

DOI: 10.1021/jacs.9b06669
J. Am. Chem. Soc. 2019, 141, 16706−16725

potential energy landscape, without prior knowledge of the final states along the reaction pathway.[49] Using the HEF approach, the facile and highly anisotropic nature of Li diffusion in $TiNb_2O_7$ is rationalized. In principle, established double-ended transition state searching methods such as the nudged elastic band (NEB) approach[50,51] can also be used to determine the activation barrier for e.g. lithium or sodium hopping[52] when the initial and final states along the conduction pathway are known, such as in layered oxides and spinels with well-defined ionic diffusion pathways. However, given the lack of prior knowledge of the transition and final states along the reaction pathways in $TiNb_2O_7$, the HEF approach is more appropriate for initial exploration of the landscape.

There have been a few reports on Na^+ intercalation into $TiNb_2O_7$, in which the bulk material exhibited very low capacity, although the performance could be improved by nanosizing of the particles.[53−56] There have been a dearth of reports of intercalation of other promising "beyond Li ion" cations such as K^+ and Mg^{2+} into the $TiNb_2O_7$ structure, and yet this, and related phases, show tunnel structures that should be able to accommodate these ions. After establishing the HEF theoretical framework to determine lithium mobility, it is straightforward to extend the method to other intercalants, as illustrated in this work.

Overall the work shows that the high-rate capability of $TiNb_2O_7$ is related to rapid lithium mobility within the Wadsley−Roth block motifs down the tunnels along the *b* axis and also between intrablock tunnels. The specific activation energies are a function of the Ti/Nb ordering; however, irrespective of cation ordering, cross-block diffusion is negligible due to the high electrostatic repulsion at the shear planes of edge-sharing octahedra. Electronically, the structure undergoes a transition from (partially) localized to delocalized behavior as the concentration of lithium increases, with evidence that localization occurs primarily on titanium.

EXPERIMENTAL AND COMPUTATIONAL METHODS

Synthesis. The samples investigated in this work were prepared by ball-milling a 1:1 stoichiometric ratio of TiO_2 (Alfa, 99.9%, anatase) and Nb_2O_5 (Alfa, 99.9985%, H polymorph) for 90 min in a zirconia ball mill (Spex 8000 M Mixer/Mill), pressing the powder into pellets at 600 MPa with a stainless-steel die set, sanding the pellet surfaces, and heating the pellets in air at 1623 K for 96 h with a 10 K min^{-1} heating rate and natural cooling in the furnace (Carbolite, HTF 1700).

X-ray Diffraction. Phase purity was examined by X-ray diffraction on a laboratory Panalytical Empyrean diffractometer with a Cu Kα source and a rotating sample stage in Bragg−Brentano reflection geometry. The data were recorded from 5 to 80° 2θ in steps of 0.0167° at a rate of 3.75° min^{-1}. Data analysis and Rietveld refinement[57] were performed with GSAS-II,[58] and the structure visualization utilized VESTA 3.4.[59]

Scanning Electron Microscopy (SEM). SEM was conducted on a Sigma VP instrument (Zeiss) at 3.0 kV with secondary electron detection. To prepare the sample, $TiNb_2O_7$ powder was suspended in ethanol and dropped from a pipette onto a holey-carbon Cu-grid TEM sample holder.

X-ray Photoelectron Spectroscopy (XPS). A Kratos Axis Ultra instrument was used to perform XPS with a monochromatic Al Kα source at 14.87 keV. Photoelectrons at pass energies of 80 eV were detected with a multichannel detector. The spectrum was analyzed using the CasaXPS software.

Diffuse Reflectance Spectroscopy. UV−visible spectrophotometry was measured with a Varian Cary 50 Bio instrument from 200 to 800 nm wavelengths. The sample was measured as a dry powder dispersed onto a quartz slide; the background was subtracted, and three measurements were averaged.

Tap Density. Powder tap density was recorded on an AutoTap (Quantachrome Instruments) instrument operating at 257 taps per minute. The measurement was performed according to ASTM international standard B527-15, modified to accommodate a 10 cm^3 graduated cylinder.

Electrochemistry. Composite electrode films for electrode performance studies were prepared with bulk $TiNb_2O_7$ powder, conductive carbon (Super P, Timcal), and a polymeric binder (polyvinylidene difluoride, Kynar, HSV 900) in an 8:1:1 mass ratio. First, the oxide and carbon were ground together with an agate mortar and pestle. This mixture was then homogenized in a solution of PVDF dissolved in *N*-methyl-2-pyrrolidone (NMP, Sigma, 99.5%, anhydrous) to create a viscous slurry that was spread onto Cu foil with a doctor blade. Residual solvent was removed from the film by drying in a furnace at 60 °C overnight. Circular electrodes of 1.27 cm^2 were cut with a punch press with a low electrode active material loading of 1.0 mg cm^{-2} to minimize overpotentials and focus on inherent micrometer particle properties; no calendaring steps were used in this work. Pure $Li_xTiNb_2O_7$ pellet electrodes of 100−550 mg were prepared for physical property measurements and structure characterization studies by pressing the powder into circular or bar-shaped free-standing pellets at 150 MPa without the presence of any conductive additive or binding agent (up to $x \leq 3.5$). Highly lithiated samples ($x \geq 3.75$ in $Li_xTiNb_2O_7$) for ex situ spectroscopic characterization required some conductive additive and binder and were prepared as free-standing pellets in an 8:1:1 mass ratio with Super P carbon (Timcal) and polytetrafluoroethylene (PTFE, Sigma, spheres) without the use of solvents or current collectors. After cycling, pellets were extracted from the cells and rinsed three times with 2 mL of dimethyl carbonate (DMC, Sigma, ≥ 99%, anhydrous). Electrochemical testing and sample preparation were conducted in stainless-steel 2032-type coin cells or Swagelok cells (conductivity measurements only) with a lithium metal anode (99.95%, LTS Research) and 1.0 M $LiPF_6$ in ethylene carbonate/dimethyl carbonate (1/1 v/v, Sigma, battery grade) liquid electrolyte. Electrochemical measurements were performed with Biologic potentiostat/galvanostat instruments. All potentials in this work are quoted relative to Li^+/Li, and *C* rates are defined with respect to the reduction of one electron per transition metal (e.g., *C*/5 = 232.6 mA h g^{-1}/5 h = 46.5 mA g^{-1}).

Solid-State Nuclear Magnetic Resonance Spectroscopy. Measurements of ^{6}Li and ^{7}Li solid-state NMR were performed at 11.75 T (Bruker Ascend wide-bore magnet) and 16.44 T (Bruker Ultrashield wide-bore magnet) with Bruker Avance III spectrometers; variable-temperature ^{7}Li NMR experiments were conducted at 9.402 T (Bruker Ultrashield wide-bore magnet) with a Bruker Avance spectrometer. The ^{6}Li Larmor frequency is 103.0 MHz at 16.44 T and 73.60 MHz at 11.75 T. The ^{7}Li Larmor frequency is 272.1 MHz at 16.44 T, 194.4 MHz at 11.75 T, and 155.6 MHz at 9.402 T. For ambient-temperature measurements, samples were packed into a 4.0 mm ZrO_2 rotor with a Kel-F cap and measured in a Bruker 4.0 mm magic angle spinning (MAS) probe at 12.5 kHz MAS frequency. Variable-temperature (VT) NMR relaxometry was performed with a Bruker 7.0 mm laser probe with samples packed into a 7.0 mm ZrO_2 rotor with a ZrO_2 cap and spun at 4 kHz MAS frequency. Temperature calibration of these experiments was performed with KBr (Sigma, ≥ 99.0%).[60] Sample temperatures are reported with an estimated accuracy of ±10 K for 293−473 K and ±20 K for 473−973 K.[47] Higher-resolution high- and low-temperature VT NMR was performed on $Li_{0.60}TiNb_2O_7$ center-packed with polytetrafluoroethylene (PTFE) ribbon in a 4.0 mm ZrO_2 rotor with a ZrO_2 cap and spun at 10 kHz MAS frequency. Temperature calibration of the 4.0 mm probe measurements was performed ex situ with $Pb(NO_3)_2$ (Sigma) with an estimated accuracy of ±5 K. One-dimensional ^{7}Li experiments at 9.402 T were performed with a 2.5 μs $\pi/2$ excitation pulse and a recycle delay of 1.5−3.0 s, based on the observed T_1

DOI: 10.1021/jacs.9b06669
J. Am. Chem. Soc. 2019, 141, 16706−16725

relaxation such that the recycle delay was always greater than $5T_1$ to ensure ≥99.3% quantitative spectra. T_1 relaxation times were measured with a saturation recovery pulse sequence. One-dimensional ^{6}Li and ^{7}Li spectra at 11.75 T were recorded with 1.0 and 2.0 μs $\pi/2$ pulses and relaxation delays of 3−20 and 5 s, respectively. Phase-cycled single pulse ($\pi/2$−acquire) and rotor-synchronized Hahn echo ($\pi/2-\tau-\pi-\tau$−acquire) experiments were performed. Due to the low natural abundance (nonenriched samples) and low Larmor frequency of ^{6}Li, between 512 and 18828 time-domain free induction decays (FIDs) were coadded before Fourier transform to achieve signal to noise (S/N) >50. For all ^{7}Li 1D spectra, 64 scans were sufficient for S/N >500 for the central transition. ^{6}Li and ^{7}Li NMR shifts were externally referenced to a 1.0 M aqueous solution of LiCl at 0.0 ppm.

The isotropic shift δ_{iso} is defined in the Haeberlen convention $\delta_{iso} = \frac{\delta_{XX}+\delta_{YY}+\delta_{ZZ}}{3}$ with the chemical shift anisotropy CSA taken as CSA = $\delta_{ZZ} - \delta_{iso}$ and the shift asymmetry η_{CSA} given by $\eta_{CSA} = \frac{\delta_{YY}-\delta_{XX}}{\delta_{ZZ}-\delta_{iso}}$. In this definition, the principal components of the shift tensor are ordered such that $|\delta_{ZZ} - \delta_{iso}| \geq |\delta_{XX} - \delta_{iso}| \geq |\delta_{YY} - \delta_{iso}|$. *N.b.*: this definition of CSA is sometimes referred to as the reduced anisotropy, which is equal to two-thirds of the "full" anisotropy $\delta_{ZZ} - \frac{\delta_{XX}+\delta_{YY}}{2}$ used by some authors and programs. The quadrupolar coupling constant C_Q is defined by the nuclear quadrupole moment Q ($Q_{Li\text{-}7}$ = −4.00(3) fm^2)[61] and the largest principal component of the electric field gradient (EFG) at the nucleus V_{ZZ} according to $C_Q = \frac{eQV_{ZZ}}{h}$ where e is the electric charge and h is Planck's constant. The quadrupolar asymmetry parameter η_Q is also defined by the EFG tensor components as $\eta_Q = \frac{V_{XX}-V_{YY}}{V_{ZZ}}$ ordered such that $|V_{ZZ}| \geq |V_{YY}| \geq |V_{XX}|$.

Magnetic Susceptibility. The magnetic susceptibility of $Li_xTiNb_2O_7$ was measured with a Quantum Design Magnetic Property Measurement System 3 (MPMS) superconducting quantum interference device (SQUID) magnetometer. Samples of ∼20 mg of pure $Li_xTiNb_2O_7$ powder were packed into a polypropylene holder, snapped into a brass rod, and wrapped with a single layer of Kapton tape. Lithiated samples were packed in an argon glovebox containing less than 1 ppm of oxygen or water. Field-cooled susceptibility was measured from 400 to 2 to 400 K in an applied field of 0.1 T. The small-field approximation was used for the susceptibility, assuming $\chi(T) = dM/dH \approx M/H$, where M is the magnetization and H is the magnetic field intensity.

Electric Conductivity. The conductivity of bar pellets of $Li_xTiNb_2O_7$ were measured under vacuum from room temperature to 150 K with a home-built four-point probe apparatus. The lithiated pellets were prepared by cold pressing pure $TiNb_2O_7$, assembling the pellets into Swagelok cells vs Li metal (as above), electrochemically lithiating to a desired stoichiometry, extracting and rinsing the lithiated pellets with dimethyl carbonate in an argon glovebox, and applying contacts with a silver epoxy onto the surface of the pellet. The nominal composition of each pellet was determined coulometrically, which assumes that every electron transferred corresponds to a Li ion intercalating into the host; this assumption is reasonable over the voltage window within the stability region of the organic carbonate electrolyte and in the absence of carbon or binder.

Density Functional Theory Calculations. The computational methods and codes are outlined here; see the Supporting Information for an expanded technical description. All electronic energies and forces in this work were calculated with DFT using the Perdew−Burke−Ernzerhof (PBE) functional[62] in the VASP code[63] with projector augmented wave (PAW) pseudopotentials.[64] The energetics of Ti and Nb disorder were studied by enumerating all symmetrically distinct Ti/Nb orderings in a $Ti_3Nb_6O_{21}$ cell using the CASM package.[65,66] Changes in the electronic structure at the initial stages of lithiation were studied in a 1 × 3 × 1 supercell of $TiNb_2O_7$ produced from one of the lowest energy Ti/Nb orderings found from enumeration. To study the nature of electronic charge localization in the $TiNb_2O_7$ structure, a single electron was doped into the ordered supercell in the presence of a charge-neutralizing background. As it has previously been demonstrated that standard DFT fails to predict the correct localization behavior of electronic charge in analogous systems such as TiO_2[67,68] and $Nb_{12}O_{29}$,[69] the electronic structure was also studied with the inclusion of a Hubbard U correction (DFT+U).[70] The rotationally invariant form of DFT+U proposed by Liechtenstein et al. was used with the PBE functional (PBE+U).[71] U values of 5.2 eV were applied to Ti and Nb ($U_{Ti:Nb}$) or Ti only (U_{Ti}). An exchange parameter, J, of 1 eV was applied in both cases. To create a distortion of the lattice to promote polaron localization, ab initio molecular dynamics (AIMD) calculations were performed with either PBE or PBE+U at 400 K.[72]

Single-ended transition state searches of Li transport were performed using the hybrid eigenvector following (HEF) approach[49,73,74] in the OPTIM code, with energies and forces taken from VASP using standard PBE. For an initial input structure, the HEF approach uses a variational procedure to find the smallest Hessian eigenvalue and corresponding eigenvector by minimizing the Rayleigh−Ritz ratio, followed by tangent space minimization as outlined in ref 73. The eigenvectors found by the variational procedure are then followed uphill until the transition state is reached. Once the transition state geometry has been located, the corresponding minima are found by displacing atoms at the transition state along the transition state eigenvector in the positive and negative directions followed by optimization of the atomic positions. The energies of the transition state, E_T, and initial and final minima, $E_{initial}$ and E_{final}, respectively, are computed with the single-ended HEF approach without previous knowledge of the final state.

The ^{7}Li paramagnetic NMR properties of the different local Li environments in the $TiNb_2O_7$ supercell were calculated with the VASP code with standard PBE according to the methodology as described in detail in previous studies.[75−77] The size of the Fermi contact shift on ^{7}Li was predicted by calculating the unpaired spin density, $\rho_N(0)$, at the Li nuclear position in the ferromagnetic state with nominally 0 K DFT. $\rho_N(0)$ can be related to the isotropic hyperfine coupling constant A_{iso} as outlined in refs 75 and 78. The value of A_{iso} at 0 K was then scaled into the paramagnetic regime with a scaling factor, Φ, to give an isotropic Fermi contact shift, δ_{iso}, via the relation $\delta_{iso} = \frac{10^6 A_{iso}\Phi}{2h\nu_0}$, where ν_0 is the Larmor frequency of ^{7}Li.[75] For a system with Curie−Weiss type magnetization, Φ is defined as $\Phi(T) = \frac{B_0\mu_{eff}^2}{3k_B g_e \mu_B S(T-\Theta)}$, where g_e is the free electron g factor, μ_B is the Bohr magneton, B_0 is the external magnetic field, μ_{eff} is the effective magnetic moment, S is the formal spin, T is the temperature, and Θ is the Weiss constant. The values of δ_{iso} in this work were calculated in supercell structures with a single electron on a d^1 transition metal, and so the formal spin-only values of S = 1/2 and μ_{eff} = 1.73 μ_B were used with Θ set to 0 K. A value of T = 340 K was used to account for frictional heating during MAS. The anisotropic components of the hyperfine tensor, $\mathbf{A}_D$, were also calculated at 0 K and scaled into the paramagnetic regime with Φ, analogous to the equation for δ_{iso}, to give the electron−nuclear dipolar shift components, δ_D^{ii} where $ii = xx$, yy, zz corresponds to the principal axis of the tensor.[75,78] The reduced electron−nuclear dipolar anisotropy, $\Delta\delta_D$, and asymmetry, η_D, are defined analogously to CSA and η_{CSA}. In addition to the hyperfine parameters, the EFG tensor $\mathbf{V}$ at the ^{7}Li nucleus was also calculated and used to compute C_Q.

RESULTS

Electrochemical Features and Lithium Ion Battery Performance of Bulk $TiNb_2O_7$. The electrochemical properties of $TiNb_2O_7$ have been reported for a variety of particle sizes/morphologies and electrode preparations.[79,24,28,37,80] In this work, a series of analytical and performance tests on undoped, bulk $TiNb_2O_7$ establish a base from which to understand our experimental and computational results on the inherent or native host properties of the material. The material

DOI: 10.1021/jacs.9b06669
J. Am. Chem. Soc. 2019, 141, 16706−16725

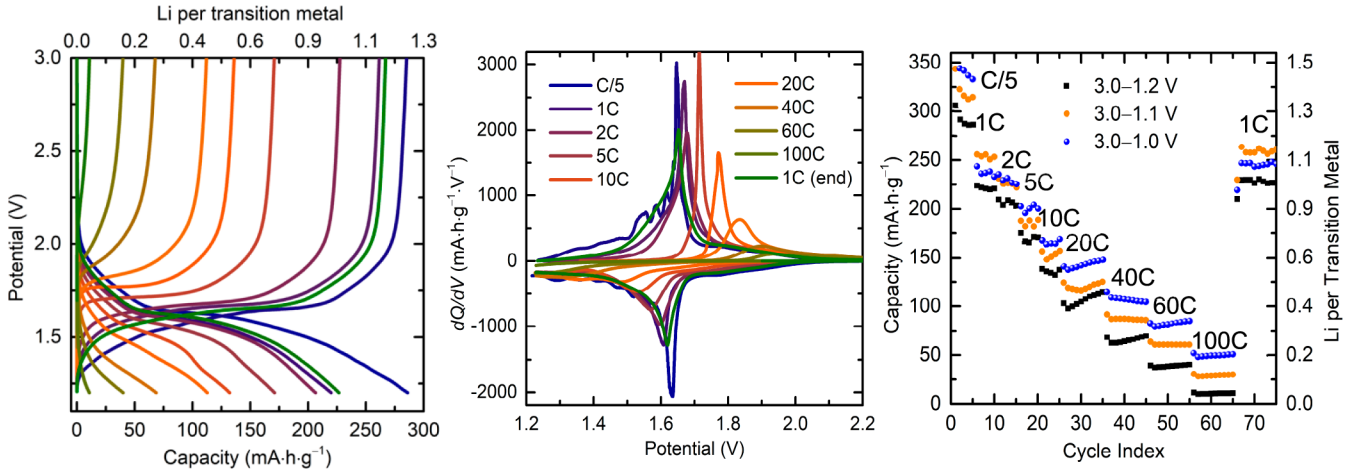

Figure 2. Electrochemical profiles and performance of $TiNb_2O_7$ vs Li as a function of rate from *C*/5 to 100*C*. (a) Galvanostatic potential vs capacity profiles and (b) d*Q*/d*V* curves. In the d*Q*/d*V* plot, discharge curves have negative values and charge curves have positive values. (c) Rate test data under galvanostatic conditions with no potentiostatic hold (i.e., CC cycling) obtained on cycling the materials from 3.0 V to 1.0, 1.1, and 1.2 V. The discharge and charge curves in (a) and (b) correspond to the middle cycle of the variable rate data in (c) with a lower voltage cutoff limit of 1.2 V.

was prepared with standard high-temperature solid-state synthesis methods and analyzed for phase and compositional purity with powder X-ray diffraction and X-ray photoelectron spectroscopy (Figure S1 in the Supporting Information). Electrodes of micrometer-scale $TiNb_2O_7$ particles (Figures S2 and S3 in the Supporting Information) with a tap density of 2.8(1) g cm^{-3} were assembled in standard coin cells and cycled against lithium metal. Electrodes with low areal mass loading levels were used to explore the inherent properties of these micrometer-sized particles. At a modest rate of *C*/5, the discharge and charge profiles (Figure 2a) can be divided into three regions: (i) an initial sloping profile for ca. 60 mA h g^{-1}, (ii) a flatter, "plateau-like" region until ca. 150−200 mA h g^{-1}, and (iii) another sloping region that extends into the multielectron redox region beyond 232.6 mA h g^{-1} and continues below 1.0 V (Figure S4 in the Supporting Information). X-ray absorption spectra at the Ti and Nb K-edges indicate that both titanium and niobium are simultaneously reduced throughout discharge.[28] These regions can also be observed in the derivative plot (Figure 2b). Though we reserve the discussion until later in the text, we note here that the electrochemical regions are less well-defined in $TiNb_2O_7$ than in some other cs phases. The charge storage capacity attained at *C*/5 was between 300 and 350 mA h g^{-1}, depending on the lower voltage limit (V_{min}) (Figure 2c). The accessible capacity drops noticeably to 225−250 mA h g^{-1} at 2*C*, decreasing further at higher rates but maintaining 100−140 mA h g^{-1} at 20C. The bulk particles are also stable for at least 1000 cycles with >90% capacity retention (Supplementary Figure S5). Similarly to several other niobium-based oxides,[21,23,81] the electrochemical results suggest that, under these conditions, there is little apparent benefit from nanostructuring these materials for energy storage applications. The influence of mass loading, electrode calendering, and various carbon or electrolyte additives are important to optimize battery performance but are outside the scope of this fundamental study.

Electronic and Magnetic Evolution. The reaction of lithium with $TiNb_2O_7$ to form ca. $Li_{0.80}TiNb_2O_7$ is associated with a sloping voltage region from the start of discharge (~2.0 V) to 1.66(1) V. Magnetic susceptibility (χ) measurements (Figure 3 and Figure S6 in the Supporting Information) indicate paramagnetic behavior in this region: the Curie constant (*C*), which measures the localized paramagnetism, increases linearly with introduced electrons, and thus lithium content, at low lithium concentrations. Beyond ca. $Li_{0.75}TiNb_2O_7$, the temperature-independent contribution (χ_0) to the total magnetic susceptibility increases (Figure 3). Despite the increase in *d* electrons at higher lithiation, the absolute magnitude of *C* is less for $Li_{1.50}TiNb_2O_7$ than for the less lithiated samples. This effect is even more dramatic when the localized paramagnetic contribution is normalized to the number of lithium and electrons transferred (*C* per Li). The increase in χ_0 and decrease in *C* are both signatures of the emergence of Pauli paramagnetism from delocalized electrons. Overall, $Li_xTiNb_2O_7$ evolves from a diamagnetic insulator at $x = 0$ to host variable amounts of localized and delocalized electrons as a function of lithium content. On the basis of the magnetic measurements, the proportion of localized electrons is largest for low lithium contents, while at high lithium contents, most electrons delocalize. This suggests the emergence of metallic conductivity upon electrochemical lithiation.

Four-point probe resistivity (ρ) measurements were recorded for $Li_xTiNb_2O_7$ as a function of lithium content on non-sintered, polycrystalline, cold-pressed bar pellets (Table 1). From the previous measurements of Xing et al., a room-temperature resistivity for $TiNb_2O_7$ of 10^9 Ω cm can be predicted.[82] However, upon lithiation to $Li_{0.25}TiNb_2O_7$ (0.083 Li/TM, 19 mA h g^{-1}) the room temperature resistivity is 5×10^1 Ω cm (Table 1 and Figure S7 in the Supporting Information), a decrease of over seven orders of magnitude. Clearly the n-doping of insulating d^0 $TiNb_2O_7$ via electrochemical reduction increases the carrier concentration to convert this electronic insulator into an effective conductor.

The lithiated polycrystalline samples were not hot-pressed out of concern for stability at the high temperatures required for densification of refractory oxides. It is thus likely that there is a significant grain boundary contribution to the measured resistances and the values reported here really represent a lower limit on the inherent conductivity of $Li_xTiNb_2O_7$. Cava et al. observed that resistivity measurements on non-sintered,

DOI: 10.1021/jacs.9b06669
J. Am. Chem. Soc. 2019, 141, 16706−16725

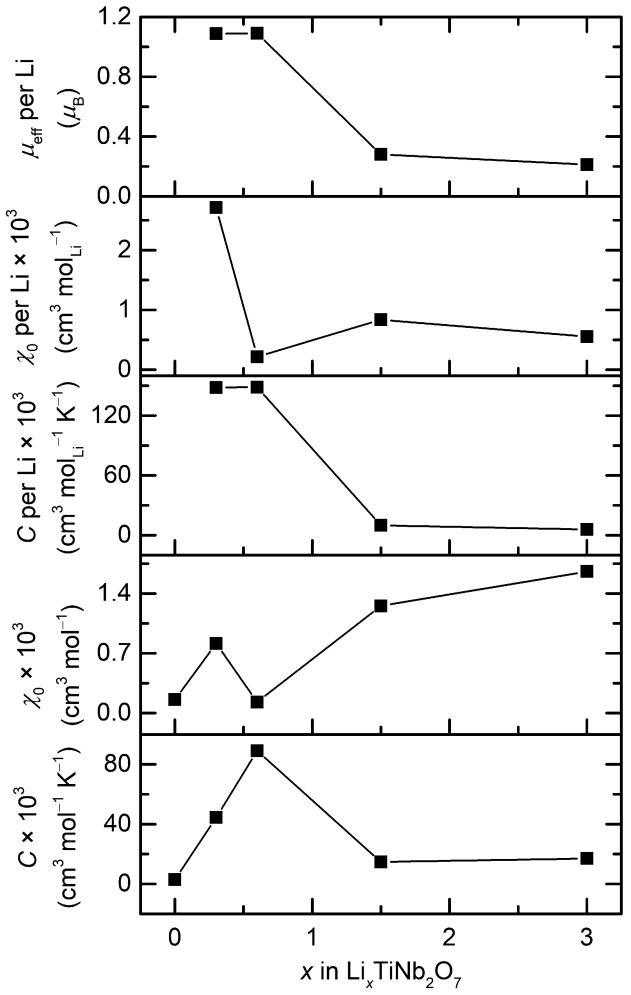

Figure 3. Magnetic constants of $Li_xTiNb_2O_7$. The temperature-dependent Curie constant (C) and temperature-independent contribution to magnetic susceptibility (χ_0) are shown normalized to the amount of sample (mol^{-1}) and of lithium (mol_{Li}^{-1}); the latter is equivalent to the number of d^1 electrons in the system. The effective magnetic moment per lithium (i.e., per d^1 electron) indicates partial Curie–Weiss paramagnetism at low x and nearly zero Curie–Weiss paramagnetic contribution at high x.

Table 1. Room-Temperature Resistivity of $Li_xTiNb_2O_7$

nominal composition	Li/TM	capacity (mA h g^{-1})	resistivity @ 294 K (Ω cm)
$TiNb_2O_7$	0	0	1×10^{9a}
$Li_{0.25}TiNb_2O_7$	0.083	19	5×10^1
$Li_{0.50}TiNb_2O_7$	0.17	39	1×10^2
$Li_{1.00}TiNb_2O_7$	0.33	78	7×10^2
$Li_{1.50}TiNb_2O_7$	0.50	116	2×10^3
$Li_{2.25}TiNb_2O_7$	0.75	174	2×10^3
$Li_{3.00}TiNb_2O_7$	1.00	233	8×10^2

[a]Room-temperature resistivity of $TiNb_2O_7$ extrapolated from 450–1100 °C data of Xing et al.[82] This polycrystalline sample was sintered at high temperatures; the lithiated samples were not sintered.

polycrystalline, cold-pressed bar pellets of crystallographic shear niobium oxides typically exhibit resistivity that is two orders of magnitude higher than would be measured on single crystals and one order of magnitude higher than would be measured on a sintered pellet.[83] The resistivity appears to increase for greater lithiation, but this too may have microstructural origins related to grain boundaries and/or pellet expansion. These effects account for the fact that the bulk resistivity measurements do not show the metallic temperature dependence that would have been expected on the basis of the magnetic susceptibility measurements. Nevertheless, the resistivities of all samples over the range $Li_{0.25}TiNb_2O_7$ to $Li_{3.00}TiNb_2O_7$ are many orders of magnitude lower than that of the host compound and compare favorably with other electrode materials.[84] The conductivity of highly lithiated $TiNb_2O_7$ is quantitatively similar to the measurement that Cava et al. recorded on lithiated H–Nb_2O_5, which exhibited a room-temperature resistivity of 4×10^3 Ω cm for H-$Li_{1.8}Nb_2O_5$.[83]

Electronic Structure Calculations. *Cation Ordering.* Partial ordering of Ti and Nb ions over the five distinct transition metal sites (M_1–M_5; Figure 1) has been observed from single-crystal X-ray and powder neutron diffraction studies of $TiNb_2O_7$.[35,85,86] In this work, the cation ordering was investigated from first-principles calculations with the PBE functional in a 30-atom ($Ti_3Nb_6O_{21}$) cell (Figure 1b) to determine the enthalpic ground-state host structure. The connectivity of the adjacent 3 × 3 blocks leads to two different types of tunnels along the b axis of the cell, labeled T1 and T2 in Figure 1b. Two Ti^{4+} ions occupied the M_5 metal sites at the edge of tunnel T2 in the four lowest energy structures, which is consistent with the experimental studies. In the enumerated structures, the third Ti^{4+} ion occupied one of the possible M_1–M_4 sites. In the lowest energy structure, the M_4 site on the edge of the ReO_3-like block was occupied by Ti^{4+}, although the energy difference between the other structures with Ti^{4+} at the M_1 (40 meV f.u.$^{-1}$), M_2 (20 meV f.u.$^{-1}$), or M_3 (30 meV f.u.$^{-1}$) sites was small. The highest energy structure contained Ti^{4+} ions solely on the M_1 and M_2 sites, and was 660 meV f.u.$^{-1}$ above the ground state. At the synthesis temperature of 1623 K, the thermal energy is approximately 140 meV, which suggests that there will be significant disorder between Ti^{4+} and Nb^{5+}, particularly on the M_1–M_4 sites.

Electronic Structure. It has been previously shown that, on lithiation, the Ti^{4+} and Nb^{5+} species are both reduced as electrons are introduced into the structure,[28] with Mulliken charges suggesting a greater degree of reduction taking place on the metal sites at the corners of the blocks (M_3 and M_5).[35] In transition-metal oxides, the localization of charge is often accompanied by a local distortion of the lattice, forming a polaron defect. To study the changes in the electronic structure on initial reduction, an "ordered" 1 × 3 × 1 supercell of $TiNb_2O_7$ containing Ti^{4+} ions on the M_5 and M_1 sites was used. This structure was chosen over the marginally lower energy Ti/Nb ordering with Ti on M_5 and M_4 sites, due to the higher symmetry of the former case, which decreased the number of inequivalent M sites. A second, "disordered" 1 × 3 × 1 supercell was also created in which the Ti and Nb ions were randomly distributed over the Ti and Nb sites. After full structural optimization with the PBE functional, the energy of the disordered $TiNb_2O_7$ cell was only 80 meV f.u.$^{-1}$ higher in energy than the lowest energy $TiNb_2O_7$ structure found previously. A single electron was then doped into the ordered and disordered structures in the presence of a charge-neutralizing background. A local distortion of the lattice was produced with AIMD at 400 K (see Supplementary Methods in the Supporting Information), followed by optimization of

DOI: 10.1021/jacs.9b06669
J. Am. Chem. Soc. 2019, 141, 16706–16725

the atomic positions with PBE or PBE+U (U_{Ti} = 5.2 eV and $U_{Ti:Nb}$ = 5.2 eV). The lattice parameters for both systems were fixed to the undoped cell as optimized with PBE. The densities of states of the optimized structures are shown in Figure 4 and Figure S8 in the Supporting Information.

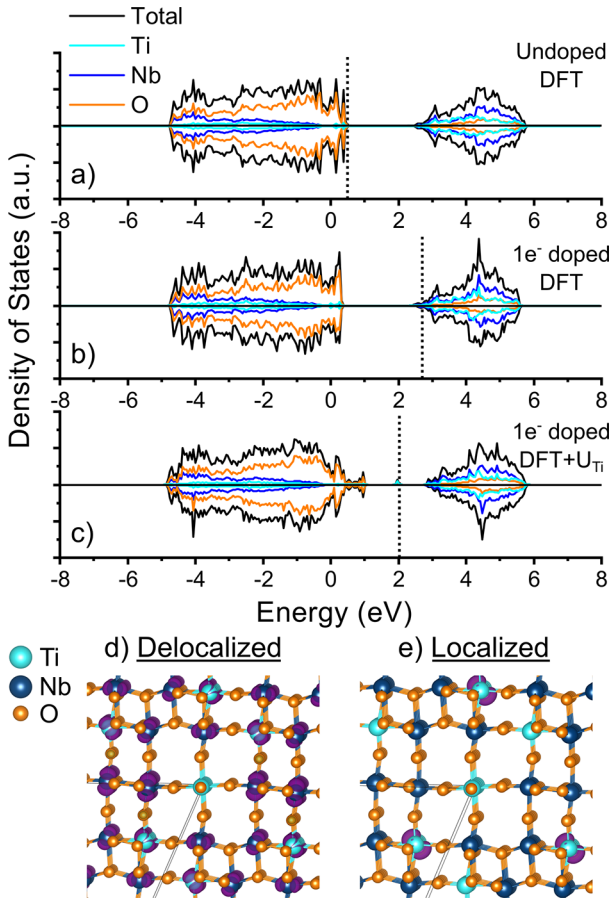

Figure 4. Density of states (DOS) for (a) pristine and (b) electron-doped $TiNb_2O_7$ supercell calculated with the PBE functional. (c) DOS of the electron-doped structure calculated with a Hubbard U correction on Ti (U_{Ti} = 5.2 eV). An enlarged view of the localized polaron state within the gap is shown with a red box. The dashed black line indicates the Fermi energy (E_F). Magnetization density isosurface for (d) delocalized and (e) localized electronic states predicted with PBE and PBE+U, respectively. Spin density isosurfaces are shown in purple. Isosurface levels of 0.001 and 0.005 a_0^{-3} were used for (d) and (e), respectively. The gray lines in (d) and (e) indicate the edges of the unit cell.

For the pristine ordered $TiNb_2O_7$ structure without an additional electron (Figure 4a), the electronic structure calculated with PBE has an optical gap of 1.87 eV between the valence and conduction bands, which is consistent with previous DFT studies.[87] The underestimation of the energy gap in comparison to the experimentally measured optical gap (3.06 eV, Figure S9 in the Supporting Information) is due to the self-interaction error in standard DFT leading to an overly delocalized wave function.

The introduction of an electron into the ordered $TiNb_2O_7$ structure results in a metallic state. During the AIMD calculation there was a partial localization of the electron spin (~0.1 e^-) on the M_5 sites on the edges of the tunnels as a result of local bond distortions. After structural optimization with standard DFT, a spin-polarized state at the bottom of the conduction band was formed (Figure 4b). The magnetization density of the DFT structure (Figure 4d) is delocalized over multiple Ti/Nb sites, forming a spin-polarized metallic state. The greatest amount of spin density is again localized on the M_5 sites at the edge of tunnel T2, with the least spin density on the M_1 sites in the center of tunnel T1. The formation of a similar spin-polarized metallic state is also observed for the disordered $TiNb_2O_7$ supercell calculated with standard DFT (Figure S10 in the Supporting Information).

For both the ordered and disordered structures, the addition of a U correction results in a localized electronic state within the original energy gap. In the ordered $TiNb_2O_7$ structure, U_{Ti} (Figure 4c) or $U_{Ti:Nb}$ (Figure S8 in the Supporting Information) corrections lead to a localized state that is primarily of Ti character from the DOS, with integrated local magnetic moments of 0.83 and 0.85 μ_B, respectively. The magnetization density (purple) of the structure with U_{Ti} = 5.2 eV is shown in Figure 4e. A localization of the magnetization is clearly present on a single Ti at the M_5 site, which is coupled to an elongation of the Ti−O bonds (Table S1 in the Supporting Information), corresponding to the formation of a small polaron. By starting the structural optimization from the metallic DFT structure obtained with PBE, it was also possible to stabilize a spin-polarized metallic state, analogous to Figure 4b, for a structure with a U_{Ti} correction applied. The resulting delocalized state was 0.101 eV higher in energy than the localized, polaron state.

In the disordered structure, the application of a U_{Ti} correction resulted in a localized polaron on an M_3 site at the corner of tunnel T1, as shown in Figure S10b in the Supporting Information, with a local magnetic moment of 0.87 μ_B. Application of a U correction on both Ti and Nb ($U_{Ti:Nb}$), resulted in a localized polaron on two adjacent M_5 Nb sites (Figure S10c in the Supporting Information). The magnetic moments of the two Nb sites in the polaron state were 0.33 and 0.36 μ_B.

The localization of charge with the application of a U parameter, as opposed to the metallic state found with standard DFT, is more consistent with the localized magnetic moments observed from magnetic measurements and the Li NMR spectra (vide infra). Although a spin-polarized state is not obtained with standard DFT, the preferential reduction of the different M sites is still in qualitative agreement with previous hybrid DFT studies.[35] The exact location of polaron defects in the $TiNb_2O_7$ structure is sensitive to the initial structure and nature of the U correction, and the different site preference between the ordered and disordered cells also suggests that the local Ti/Nb environments will affect the charge localization.

Lithium Solid-State NMR Spectroscopy. To understand the lithium insertion process of $TiNb_2O_7$, ^6Li and ^7Li solid-state MAS NMR spectra were recorded as a function of lithium content from $Li_{0.10}TiNb_2O_7$ (0.033 Li/TM) to $Li_{5.50}TiNb_2O_7$ (1.83 Li/TM) (Figure 5). At the start of discharge a ^7Li resonance is observed at the composition $Li_{0.10}TiNb_2O_7$ that fits well to a single Gaussian−Lorentzian (pseudo-Voigt) line (Figure S11 in the Supporting Information). Upon further lithiation, two resonances are observed; the major signal (ca. 90% integrated intensity) shifts to lower frequencies on increasing lithiation, reaching −10.7 ppm at $Li_{0.60}TiNb_2O_7$ (Figure 5 and Figure S12 in the Supporting Information), which is well outside the typical range of diamagnetic lithium.

DOI: 10.1021/jacs.9b06669
J. Am. Chem. Soc. 2019, 141, 16706−16725

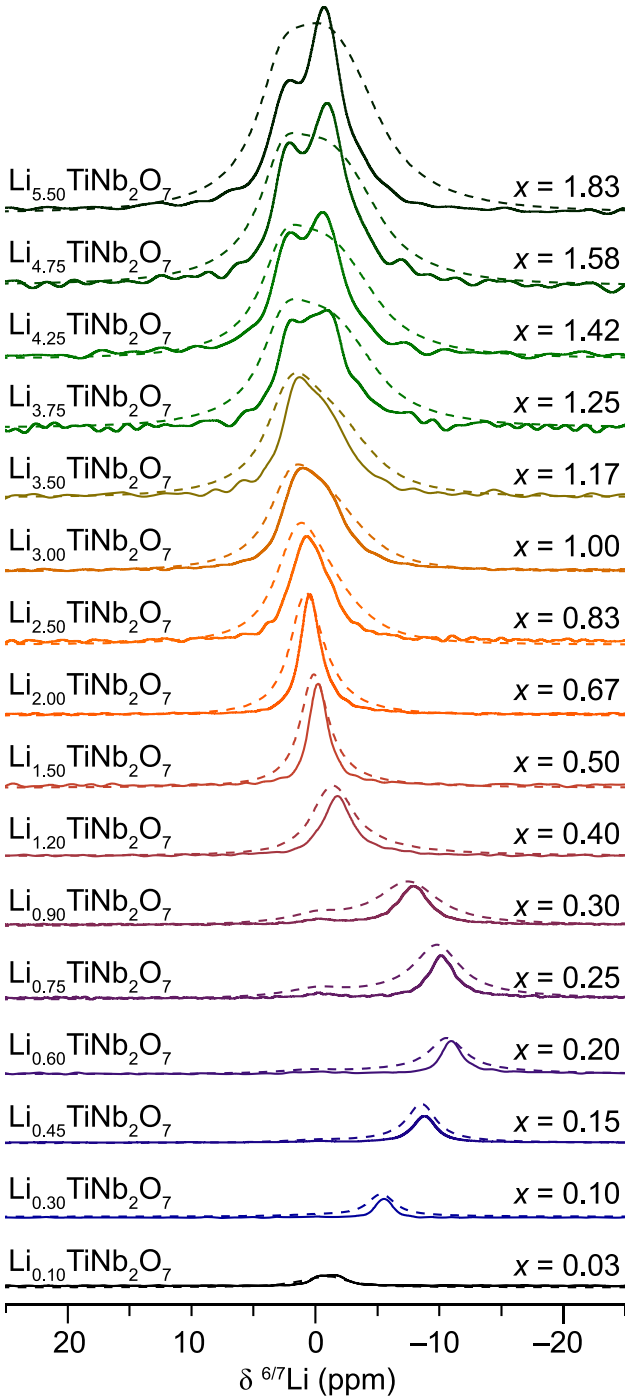

Figure 5. ^{6}Li (solid lines) and ^{7}Li (dashed lines) MAS NMR spectra of $Li_xTiNb_2O_7$. Single-pulse spectra were collected in the range x = 0.10−5.50 (8−426 mA h g^{-1}) at an MAS frequency of 12.5 kHz and B_0 = 11.7 T.

Hahn echo MAS NMR experiments also indicate a shorter T_2 spin−spin relaxation constant for the negatively shifted resonance (Figure S13 in the Supporting Information). Both the negative resonant frequency and the shorter T_2 of this signal suggest an increased paramagnetic shift contribution, arising from localized electrons on the niobium and titanium ions as they are reduced from d^0 to d^1 electronic states in the first electrochemical region. This is in agreement with the magnetic susceptibility data at low lithium content. Given the paramagnetic origin of this shift, it is then surprising to observe narrow NMR line shapes. To investigate this, high-resolution variable-temperature ^{7}Li MAS NMR spectra of $Li_{0.60}TiNb_2O_7$ were recorded below and above room temperature (Figure S14 in the Supporting Information). The low-temperature NMR spectra show dramatic broadening of the negatively shifted resonance, while the high-temperature spectra show further line narrowing. These experiments suggest that the paramagnetic resonance is partially motionally narrowed at room temperature—another indication of the lithium mobility under ambient conditions in the $TiNb_2O_7$ host material. Furthermore, the magnitude of the paramagnetic shift decreases with increasing temperature, i.e. the shift becomes less negative, confirming that the shift is paramagnetic in origin (Figure S14 in the Supporting Information).

As the structure is further lithiated, the resonance shifts back toward 0 ppm and the line shape can again be well described by a single peak for $Li_{1.20}TiNb_2O_7$. The NMR line widths (full width at half-maximum, fwhm) decrease for samples within the second, pseudoplateau-like electrochemical feature, indicating increased motional averaging.

The NMR spectra of lithium concentrations corresponding to the third, sloping region of the electrochemical profile are characterized by a broad, asymmetric signal centered around 0 ppm; this signal can be described with a simple two-component model (Figures S11 and S12 in the Supporting Information) for all lithium contents greater than $Li_2TiNb_2O_7$. While the fewest possible peaks were used to fit each NMR line shape, more lithium sites and thus resonances are expected from the crystal structure; this anomaly could be due to either very small shift differences between lithium in magnetically inequivalent sites or lithium exchange between different sites with an exchange frequency greater than the separation between their isolated NMR shifts. Both effects likely coexist in $Li_xTiNb_2O_7$ with a small shift range and rapid lithium mobility. The small shift also suggests that the Knight shift contributions, which could be core-polarization or orbital in nature, either are very small or effectively cancel out.

^{7}Li NMR spectroscopy was complemented by high-resolution ^{6}Li NMR spectroscopy (Figure 5) across the entire lithiation series: the dipolar and quadrupolar broadening mechanisms are suppressed for ^{6}Li vs ^{7}Li due to the smaller Larmor frequency and quadrupole moment, respectively, of ^{6}Li. The similarity of the isotropic resonance line width trends between ^{6}Li and ^{7}Li for $Li_xTiNb_2O_7$ is evidence that the changes in broadening are not caused by dipolar coupling between nuclei or quadrupolar coupling between the nuclear quadrupole and the electric field gradient at the nucleus but rather are due to nucleus-independent effects such as solid-state exchange kinetics and distributions of environments.

^{7}Li Paramagnetic NMR Calculations. The ^{7}Li NMR parameters of the local Li minima (Li_A−Li_G) in the ordered supercell ($LiTi_9Nb_{18}O_{63}$) were determined from first-principles calculations to aid the assignment of the experimental NMR (Table S2 in the Supporting Information and discussion therein). An in-depth discussion of the Li positions will be given below in the context of the first-principles Li diffusion calculations. All of the Li sites have a small, negative ^{7}Li NMR Fermi contact shift, ranging from −1 to −19 ppm, which is consistent with experiment, accounting for motional exchange. The different local environments in Table S2 in the Supporting Information also experience different C_Q values. The largest C_Q value is computed for the square-planar (LiO_4) site in $TiNb_2O_7$ (see Lithium Diffusion Mechanism), as it has the

DOI: 10.1021/jacs.9b06669
J. Am. Chem. Soc. 2019, 141, 16706−16725

most anisotropic local environment. Smaller C_Q values in the range of 30−70 kHz are predicted for sites with higher coordination (approximately LiO_5) that leads to a more spherical charge distribution. The experimental SSB manifold widths (Figure S15 in the Supporting Information) correspond to C_Q values of ca. 70−250 kHz, which are in partial agreement with the calculations, while they suggest that the effects of nondilute lithium content, especially above 1.0 Li/TM, lead to larger C_Q values and thus more distorted Li environments.

Variable-Temperature ^{7}Li NMR Spectroscopy. Variable-temperature NMR spectra were recorded over a large temperature range with a laser-heated probe to measure lithium mobilities and activation energies from motionally-induced nuclear relaxation, as well as to investigate line shape evolution as a function of temperature. For lithiated $TiNb_2O_7$, given the size of the quadrupolar interaction relative to homonuclear dipolar coupling under MAS, the motionally-induced fluctuations in the quadrupolar interaction dominate the T_1 relaxation, and hence the relaxation data were converted to motional correlation times (τ) according to BPP theory via the expression

$$\left(\frac{1}{T_1}\right)_Q = \frac{3}{200} C_Q{}^2 \left(1 + \frac{\eta^2}{3}\right)\left(\frac{2I+3}{I^2(2I-1)}\right) \left[\frac{\tau^2}{1+\omega_0{}^2\tau^2} + \frac{4\tau^2}{1+4\omega_0{}^2\tau^2}\right]$$

where ω_0 is the Larmor frequency, C_Q is the nuclear quadrupolar coupling constant, η is the quadrupolar asymmetry parameter, and I is the nuclear spin (I = 3/2 for ^{7}Li). This predicts that the T_1 will exhibit a minimum when $\omega_0\tau \approx 1$, from which the correlation time can be determined directly at the temperature corresponding to the T_1 minimum. The observed T_1 minima correspond to C_Q values, within this model, of 130 kHz at low lithium content to 200−210 kHz at high lithium content. In reality, there will be multiple, possibly partially averaged, quadrupolar constants for the different lithium sites and there should also be contributions to the relaxation from dipolar interactions and unpaired electrons, but the single-parameter quadrupolar model corresponds to C_Q values that are consistent with the spectra. T_1 minima were used directly to determine diffusion coefficients. The activation energies (E_a) were extracted from Arrhenius fits ($\frac{d\ln T_1}{d\left(\frac{1}{T}\right)} = \pm E_a$) to regions on either side of the T_1 minimum; temperatures below the T_1 minimum correspond to long τ, while temperatures above the T_1 minimum correspond to short τ. Obtained E_a values were very small, in the range of 20−85 meV in the low-temperature, slower hopping region ($\omega_0\tau > 1$) and 60−390 meV in the high-temperature, faster hopping region ($\omega_0\tau < 1$) (Figure 6 and Table S3 in the Supporting Information). The observed asymmetry between the long- and short-τ regimes has been ascribed to short- vs long-range mobility and differences in dimensionality, which are both relevant in the case of $TiNb_2O_7$ (see Lithium Diffusion Mechanism). The activation barrier for this lithium motion is thus within a small factor of room-temperature thermal energy (k_BT = 25.7 meV at 298 K). The activation energy for lithium hopping, especially in the high-temperature region, increases drastically at high lithium content (Table S3 in the Supporting Information). This agrees with the analysis of lithium kinetics from the galvanostatic intermittent titration technique (GITT)

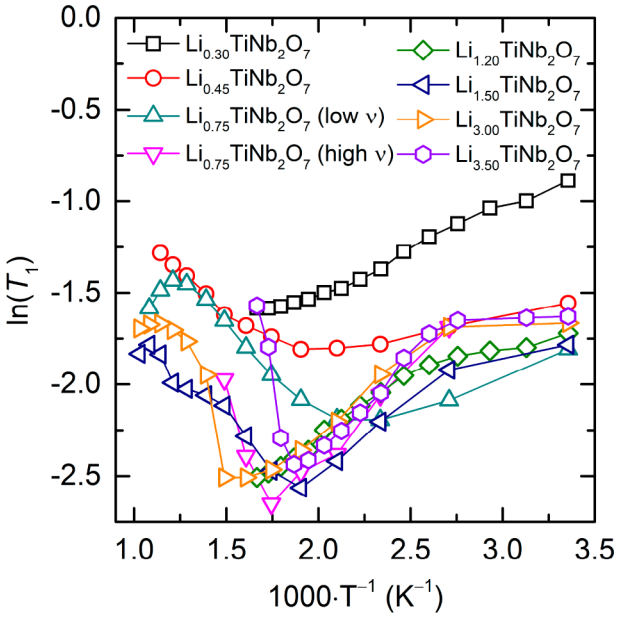

Figure 6. ^{7}Li spin−lattice relaxation constants for $Li_xTiNb_2O_7$ on an Arrhenius plot. T_1 constants at 4 kHz MAS and 9.4 T were extracted from saturation recovery experiments as a function of lithium composition and variable temperature via laser heating.

(Figure S16 in the Supporting Information), which shows that the chemical diffusion coefficient of lithium is relatively constant during lithiation until the composition reaches $Li_3TiNb_2O_7$, noting that values during the pseudoplateau feature cannot be analyzed by conventional GITT if they correspond to the presence of multiple phases.[88] The lithium diffusion in lithium-stuffed concentrations (>1 Li/TM) is nearly two orders of magnitude lower than that in lithium-dilute concentrations.

At the T_1 minima, $\omega_0\tau \approx 1$; thus, at this field the correlation time is $\tau \approx 6$ ns. This can be converted to a self-diffusion coefficient (D_{Li}) via the Einstein−Smoluchowski relation

$$D_{Li} = \frac{l^2}{2d\tau}$$

where l is the lithium hop distance and d is the dimensionality of diffusion. As we will see from the DFT calculations (vide infra), the dimensionality of local ion hopping in $TiNb_2O_7$ is restricted 3D (restricted by crystallographic shear planes), while long-range diffusion is 1D along the parallel tunnels present in all Wadsley−Roth phases. From the Einstein−Smoluchowski equation with d = 1 and l = 3.8 Å, D_{Li} in $Li_xTiNb_2O_7$ is ca. 10^{-11} m^2 s^{-1} at the temperature of the observed T_1 minimum of 525−650 K for $x \geq 0.75$.

Under these spectroscopic conditions (4 kHz MAS, 9.4 T), one asymmetric signal was resolved for all samples (Figure 7 and Figure S17−S23 in the Supporting Information) with the exception of $Li_{0.75}TiNb_2O_7$ from 370 to 670 K (Figure S18 in the Supporting Information). This sample exhibited a considerably lower temperature T_1 minimum of 425 K for the paramagnetically-shifted low-frequency peak, suggesting that this lithium reservoir at this composition is more mobile.

The ^{7}Li shifts and spinning sideband patterns undergo significant changes over the investigated temperature range (Figure 7 and Figures S17−S23 in the Supporting Information). As the temperature increases, the average

DOI: 10.1021/jacs.9b06669
J. Am. Chem. Soc. 2019, 141, 16706−16725

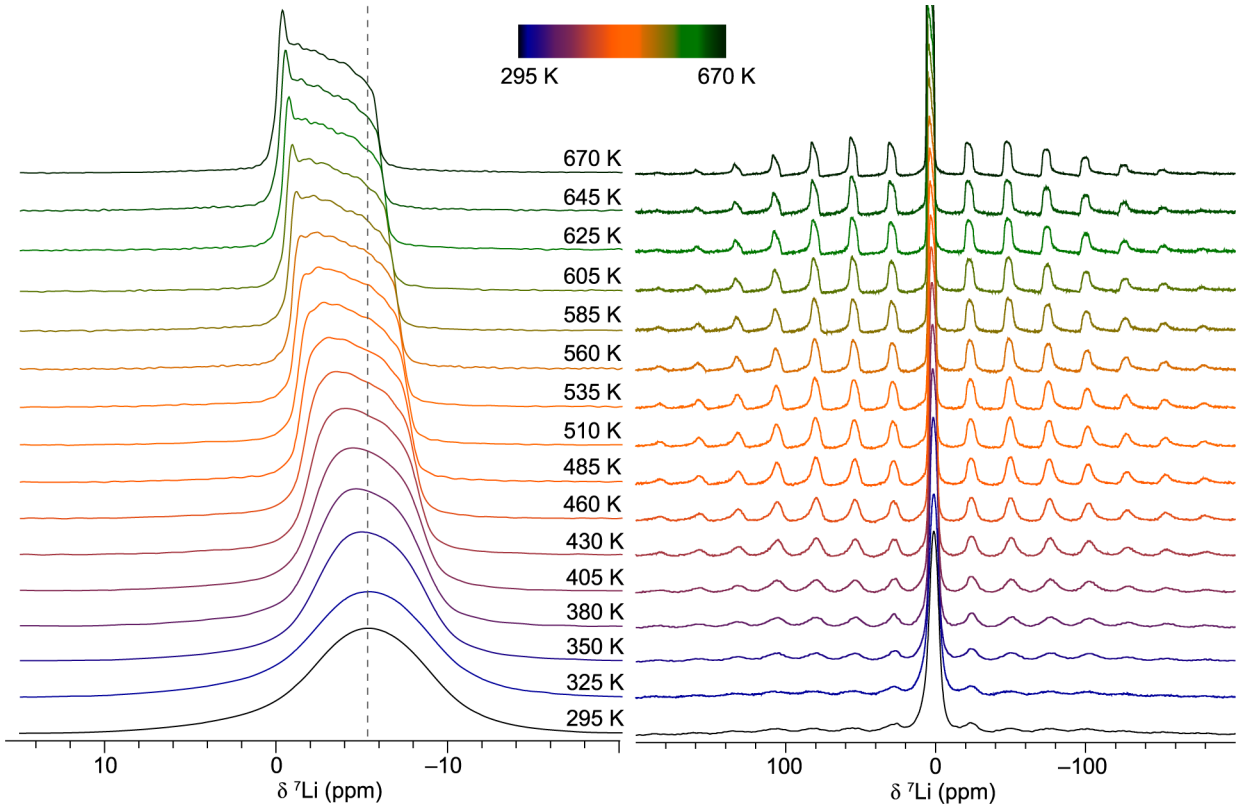

Figure 7. High-temperature ^{7}Li MAS NMR spectra of $Li_{0.30}TiNb_2O_7$. The (a) central transition and (b) spinning sideband manifold are depicted as a function of temperature from 295 to 670 K (ascending). The dashed vertical line in (a) indicates the average shift in the ambient-temperature $\delta(^{7}Li)$ spectrum. Spectra were recorded at 4 kHz MAS and 9.4 T. See also Figures S17−S22 in the Supporting Information.

frequency of the paramagnetically shifted resonances moves toward the diamagnetic region centered around zero, as expected for localized paramagnetism. The sideband evolution with temperature is complicated but hints at differential and changing dynamics. Numerical simulations of the quadrupolar powder patterns indicate that essentially the entire sideband intensity comes from the nuclear satellite transitions (−3/2 ↔ −1/2, +1/2 ↔ +3/2) for ^{7}Li (I = 3/2) in this system. As we also saw in the ambient-temperature high-resolution NMR spectra (Figure S15 in the Supporting Information), the ambient-temperature laser-probe spectra (Figure S23 in the Supporting Information) exhibit relatively small sideband patterns, and hence C_Q values, upon lithiation up to $Li_{1.50}TiNb_2O_7$; the C_Q value then increases drastically at and above $Li_{3.00}TiNb_2O_7$.

By 400−450 K, increasing sideband intensity appears for $x \leq 1.50$ in $Li_xTiNb_2O_7$, whereas the intense sideband manifold decreases for $x \geq 3.00$ at elevated temperatures. Spectral broadening occurs when the rate of exchange is of the same order of magnitude as the interaction that is being averaged by the exchange,[89−91,47] in this case quadrupolar coupling of the order 50−250 kHz. Taken together, the variable-temperature lithium NMR spectra reveal several trends in lithium mobility.

In samples with low lithium content ($x \leq 1.50$), the intercalated lithium ions are in an intermediate motional regime, with partial averaging giving rise to broad central and sideband resonances. At higher temperatures (ca. 400−600 K; Figure 7 and Figures S17−S20 in the Supporting Information), the sideband amplitude increases as the sidebands become sharp. This is attributed to averaging of the dipolar coupling (likely major) and the shift tensor (likely minor) but not of the quadrupolar coupling. At very high temperatures (ca. ≥700 K), the quadrupolar interaction is averaged and the full spectral width of the satellite transitions decreases. The onset of motional averaging shifts to higher temperatures at higher states of lithiation.

Highly lithiated $TiNb_2O_7$ (>1.50 Li/TM) experiences slower ionic mobility, as evidenced from GITT and NMR relaxometry, which results in larger quadrupolar and dipolar interactions, and hence the sideband manifold (Figures S21 and S22 in the Supporting Information) and fwhm (Figure 5) are broad at room temperature. Upon heating, the individual SSBs broaden and overlap (compare e.g. Figures S20 and S21 in the Supporting Information at intermediate temperatures). Sideband narrowing then occurs above 800 K; averaging of the quadrupolar interaction is obscured by the broadened sidebands but may also be occurring at very high temperatures. For context, motional broadening of the dipolar-broadened ^{7}Li−^{7}Li satellite transition SSBs in Li_2CO_3 does not occur until around 570 K, with motional narrowing setting in at higher temperatures.[47] Even to 970 K, only marginal averaging of the relatively small quadrupolar coupling ($C_Q \approx 70$ kHz) is observed in that relatively nonconducting system.[47]

Given the high lithium mobility of $TiNb_2O_7$, ^{7}Li pulsed field gradient (PFG) NMR spectroscopy was performed with the aim of directly measuring a macroscopic diffusion coefficient, but the short T_1 and T_2 relaxation coefficients prevented the measurement of a decaying static signal. Operando ^{7}Li NMR spectroscopy (Figure S24 in the Supporting Information) was also performed to track real-time changes and look for metastable intermediates, but the static nature of operando electrochemical NMR, combined with the small (10 ppm)

DOI: 10.1021/jacs.9b06669
J. Am. Chem. Soc. 2019, 141, 16706−16725

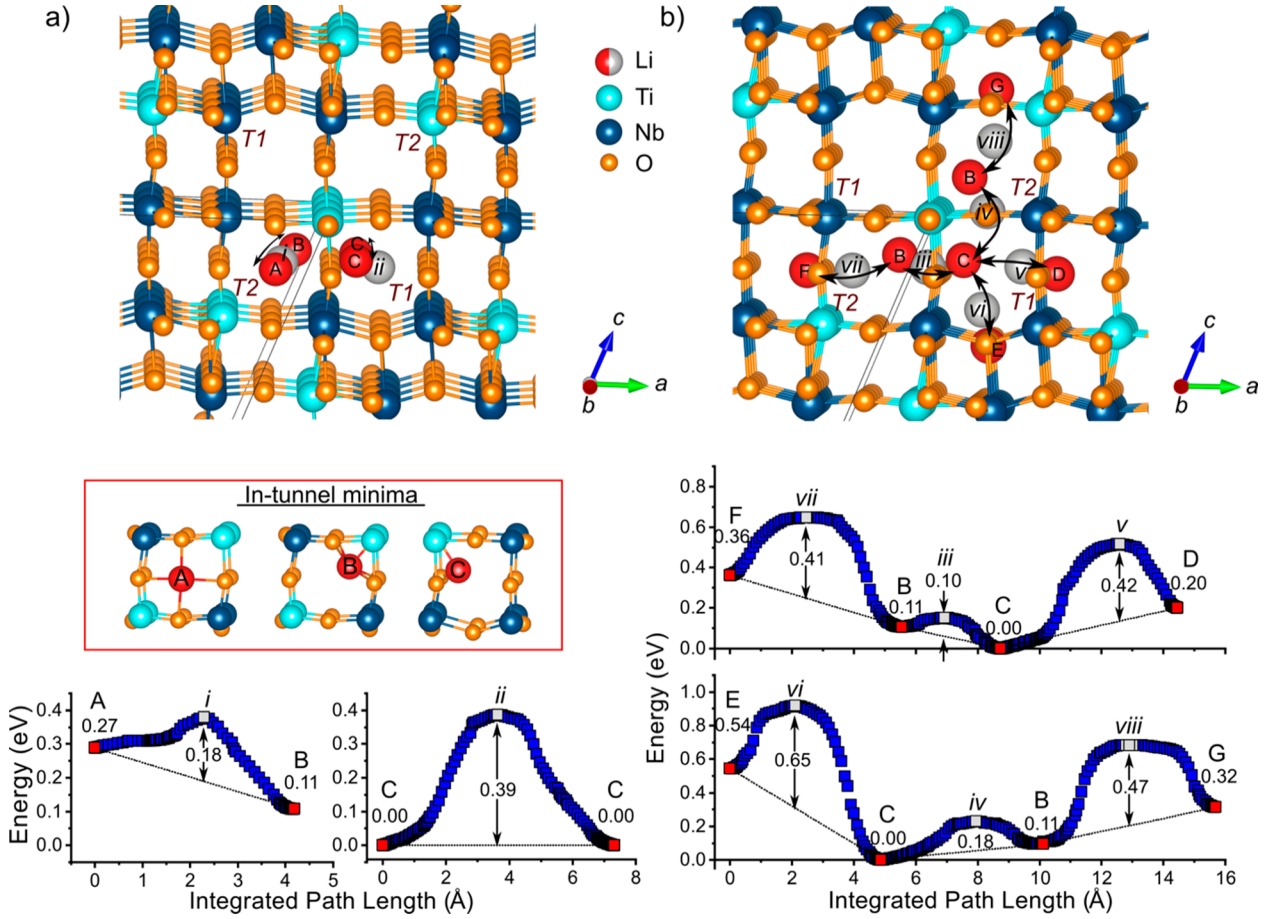

Figure 8. Li conduction pathways and corresponding activation barriers in eV located via the hybrid eigenvector following approach along the (a) *b* axis and (b) *ac* plane of an "ordered" $TiNb_2O_7$ supercell structure. Li minima (Li_A–Li_G) and transition states (configurations *i*–*viii*) are shown in red and gray, respectively. Curved black arrows show the direction of Li hops. The energies of the local minima (red squares) and kinetically-resolved activation barriers (eq 1 in the Supporting Information) to the transition states (gray squares) are shown relative to configuration C at 0 eV. An interpolation of the energy between the initial and final minima for each hop is shown. The local bonding environments of in-tunnel Li minima (Li_A–Li_C) are also displayed (red box).

isotropic shift range of $Li_xTiNb_2O_7$ that overlaps with the large electrolyte resonance, meant that no considerable changes were observed (other than in the Knight-shifted Li metal resonance at 248 ppm from varying intensity and from microstructural effects[43,92]).

Lithium Diffusion Mechanism. Previous experimental and theoretical studies have highlighted that there are multiple possible sites for Li insertion into the $TiNb_2O_7$ structure.[87,93] Catti et al. proposed that there are two main types of Li coordination: five-coordinate (LiO_5) square-pyramidal sites on the edges of the 3 × 3 blocks and four-coordinate (LiO_4) square-planar sites within the 3 × 3 block.[93] Here, first-principles calculations were used to explore the possible Li insertion sites and associated ion motion barriers. A single-ended transition state searching approach based on hybrid eigenvector following (HEF) was adopted to locate local minima and transition states in the Ti/Nb "ordered" $TiNb_2O_7$ supercell described previously. Although it was previously shown (vide supra) that the formation of localized polaron states is sensitive to the inclusion of a Hubbard *U* parameter, the description of the electronic structure without a *U* correction is in qualitative agreement with experiment. For the remainder of this study we therefore used standard DFT to capture the mechanisms associated with ionic diffusion, without the presence of additional electron transfer processes, an approach commonly adopted in other transition-metal oxide battery materials.[52]

Transition state searches were initiated by placing a single Li atom close to the center of a LiO_4 window for all possible LiO_4 and LiO_5 sites in the structure. Once the transition state was found, the corresponding minima along the reaction pathway were located by displacing the atoms along the single negative eigenvector at the saddle point in both the positive and negative directions, followed by optimization of the atomic positions. The diffusion mechanisms and associated activation barriers of the "ordered" $TiNb_2O_7$ cell are shown in Figure 8. Movies depicting the various ionic hopping pathways are included in the Supporting Information.

Within the blocks, three minima were located: sites Li_A and Li_B in tunnel T2 and site Li_C in tunnel T1, as shown in Figure 8a. Li_C is the lowest energy position in the Ti/Nb ordered $TiNb_2O_7$ supercell and corresponds to a distorted site in which the Li ion is displaced toward the center of tunnel T1. Hopping between Li_C sites along the *b* axis of the cell requires a moderate activation energy of 0.39 eV. Interestingly, in the dilute limit, the square-planar (LiO_4) site within tunnel T1 corresponds to the transition state (configuration *ii*) along the Li_C–Li_C diffusion path and not a local minimum. Site Li_B

DOI: 10.1021/jacs.9b06669
J. Am. Chem. Soc. 2019, 141, 16706–16725

adopts a five-coordinate square-pyramidal site, distorted toward the center of tunnel T2, similar to site Li_C in tunnel T1. Site Li_B is analogous to the distorted five-coordinate Li site observed at low levels of lithiation in the related compound V_6O_{13}.[94] The energy difference between the Li_B and Li_C sites (0.11 eV) is small, suggesting that both may be populated at room temperature. In tunnel T2, the square-planar site, Li_A, along the *b* axis is a local minimum, which is 0.16 eV higher in energy than the five-coordinate Li_B site. The activation energy for Li_A−Li_B diffusion (0.18 eV) is also low, suggesting that *b* axis conduction down tunnel T2 will be facile.

The conduction mechanisms between sites within the *ac* plane are shown in Figure 8b. In addition to the in-tunnel sites (Li_A−Li_C), square-pyramidal (LiO_5) sites (Li_D−Li_F) were also located with the HEF approach on the edges of the blocks, in agreement with previous studies.[87,93] In the ordered $TiNb_2O_7$ supercell, the Li_E and Li_F sites on the edges of the tunnels are the highest in energy while the Li_B and Li_C sites within the tunnels are the lowest in energy, suggesting preferential lithiation of the tunnels in the first stages of lithiation. However, as will be shown below, the relative energies of the different sites are subtly related to the Ti/Nb ordering. Within the blocks, conduction between the Li_B and Li_C sites can occur along the *a* axis or *c* axis through the square-planar (LiO_4) windows (configurations *iii* and *iv*, respectively). The small kinetically-resolved activation energies of 0.10 and 0.18 eV for *a* and *c* axis diffusion, respectively, suggest that Li^+ can rapidly diffuse between tunnels T1 and T2. The activation barriers between the square-pyramidal sites and Li_B/Li_C sites (configurations *v*−*viii*) are larger (0.41−0.65 eV), indicating that diffusion within the *ac* plane to these sites will be slower.

The square-pyramidal sites on the edges of one block share a common edge with the square-pyramidal sites in an adjacent block, creating a possible pathway for cross-block diffusion. As can be seen in Figure 9, significantly larger barriers (0.71−1.00 eV) are observed for cross-block diffusion, suggesting that these pathways do not contribute significantly to the overall diffusion process, at least at dilute levels of lithiation. At the transition state of the cross-block diffusion (configurations *ix*−*xi*), the diffusing Li^+ has a distorted-octahedral (LiO_6) configuration that is face-sharing with four transition-metal (MO_6) octahedra, resulting in a large electrostatic repulsion. This is consistent with a previous computational study on the related system TiO_2(B), in which diffusion across the tunnels is higher in energy than down-tunnel diffusion.[95] These results agree with and lend quantitative support to the simplified picture provided by bond valence sum mapping (Figure S25 in the Supporting Information).

In a real $TiNb_2O_7$ sample, the disordered arrangement of Nb and Ti sites also leads to a local distribution of neighbors for each Li site. To capture the effect of transition-metal disorder, the previously observed Li ion activation barriers in the ordered supercell were investigated in the disordered supercell. Transition state searches involving a single Li ion were initiated from all of the possible LiO_4 windows in the structure using the approach described previously. The energies of the local Li minima and activation barriers found in the disordered $TiNb_2O_7$ supercell are shown in Figure 10a,b, respectively.

The transition-metal disorder leads to a distribution of energies for all of the local minima (Li_A−Li_G) in Figure 10, which is related to the different electrostatic potential experienced by the Li ion with different arrangements of Ti^{4+}/Nb^{5+} neighbors around a given site. In the disordered

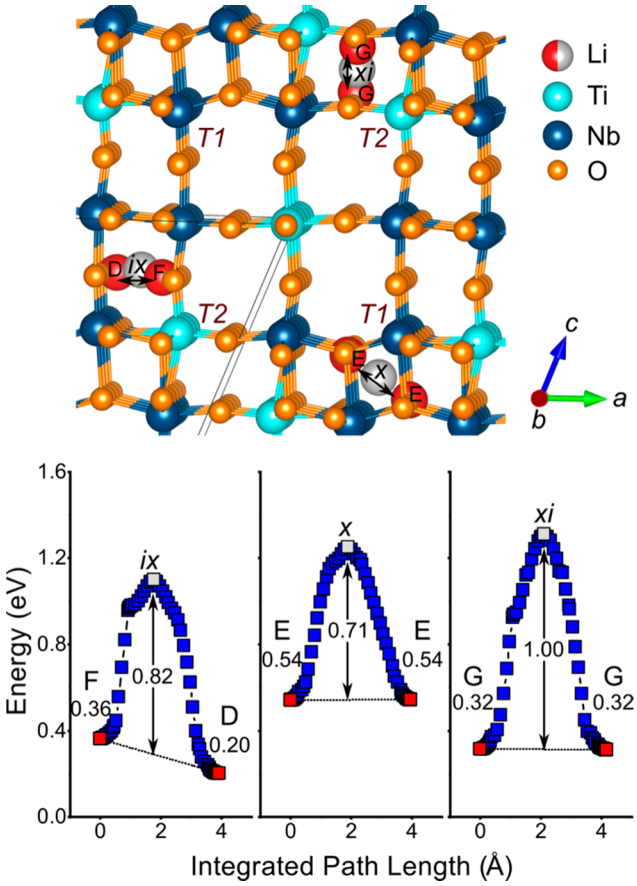

Figure 9. Cross-block Li diffusion pathways and corresponding activation energies in eV. Li minima (Li_D−Li_G) and transition states (configurations *ix*−*xi*) are shown in red and gray, respectively. The energies of the local minima and kinetically-resolved activation energies (eq 1 in the Supporting Information) relative to configuration C are displayed on the conduction barrier plots (blue). An interpolation of the energy between the initial and final minima for each Li hop is shown.

supercell, the trend in the relative site energies remains the same as that found for the ordered $TiNb_2O_7$ supercell, in which the in-tunnel environments (Li_A−Li_C) are lower in energy than the square-pyramidal environments Li_E−Li_G on the edges of the tunnels. The square-pyramidal environment Li_D on the edge of tunnel T1 was, however, found to be a low-energy site for several local Li orderings. The results above regarding the possible Li environments are only strictly applicable for dilute levels of Li doping in $TiNb_2O_7$, as Li−Li interactions and transition-metal reduction $M^{n+} \rightarrow M^{(n-1)+}$ at higher levels of Li insertion will affect the relative energies of the different sites. However, the similarity between the energies of the different Li configurations suggests that there will be a significant population of square-planar (Li_A), distorted-five-coordinate (Li_B and Li_C), and square-pyramidal (Li_D) sites on initial lithiation.

For several of the diffusion pathways connected to in-tunnel local environments (Li_B and Li_C) in the disordered supercell, the single-ended transition state searches from neighboring sites resulted in a splitting of the positions found in the ordered supercell into different local Li positions within the same tunnel (Figure S26 in the Supporting Information). The activation barrier between two split Li_C sites was calculated using the HEF approach and was found to be 0.04 eV. This

DOI: 10.1021/jacs.9b06669
J. Am. Chem. Soc. 2019, 141, 16706−16725

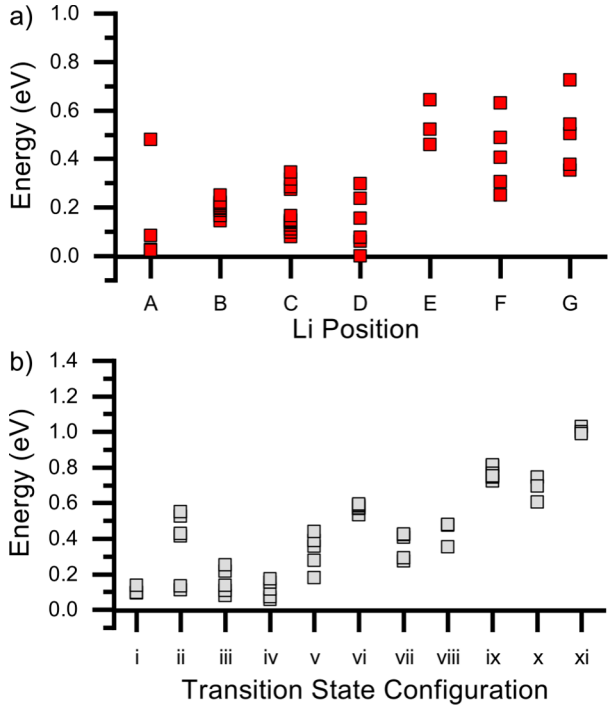

Figure 10. Energies of (a) local Li minima and (b) kinetically-resolved activation barriers in the disordered $TiNb_2O_7$ supercell. Li sites Li_A–Li_G correspond to the Li positions observed in the ordered $TiNb_2O_7$ structure in Figure 8. The energies of all minima are referenced to the lowest energy Li_D site at 0 eV.

result suggests that the presence of Ti/Nb disorder subtly changes the in-tunnel sites, creating multiple shallow local minima that can rapidly exchange. This behavior is analogous to the rapid diffusion between adjacent sites within the same block in the perovskite solid electrolyte material $Li_{3x}La_{(2/3)-x}TiO_3$ (LLTO).[96]

The trend in the relative activation energies between different diffusion mechanisms previously found in the ordered supercell remains the same in the disordered supercells (Figure 10b), with a distribution of the energies in the latter case. Activation barriers for *b* axis diffusion of 0.10–0.14 and 0.11–0.55 eV were found for configurations *i* and *ii*, respectively, using the HEF approach. From an analysis of the transition state structures of configuration *ii*, it is evident that the activation barrier for ionic conduction through the square-planar window is lowest when transition-metal site M_4 on the edge of the block is occupied by Ti^{4+}, which results in a lower electrostatic repulsion than that for Nb^{5+}. A deeper understanding of the effect of disorder and Ti/Nb local environments on the activation barriers could be gained through a cluster expansion-type approach,[65,97] although this is beyond the scope of the current study.

The activation energies of the pathways within the ReO_3-like blocks between tunnels T1 and T2 (via configurations *iii* and *iv*) remain low (0.06–0.25 eV) for all of the pathways calculated, suggesting that rapid transport between tunnels T1 and T2 will still occur for a range of different local Nb/Ti orderings. The range of activation barriers (0.18–0.44 eV) for diffusion between square-pyramidal site Li_D and site Li_C (configuration *v*) was similar to that of *b* axis diffusion, whereas the range of activation barriers for diffusion to the higher energy square-pyramidal sites (Li_E–Li_G) was larger (0.27–0.59 eV). The energy of the cross-block barriers (configurations *ix*–*xi*) remained very high (0.60–1.03 eV) for all local Ti/Nb orderings, suggesting that 3D diffusion between blocks is limited.

The change in the Li diffusion barriers at higher levels of lithiation ($Li_xTiNb_2O_7$) was investigated for a limited number of concentrations (x = 2.667, 4) in the ordered and disordered $TiNb_2O_7$ structures (Figures S27 and S28 in the Supporting Information). At higher levels of lithiation, the square-planar transition state configurations *ii* and *iii* (Figure 8) in the ReO_3-like blocks become stable sites for Li. The energy preference to create Li vacancies at different square-planar and square-pyramidal sites in the structure was found to be sensitive to both the Li composition and Ti/Nb ordering. The activation barriers for down-tunnel Li diffusion were also found to be sensitive to the Li composition with values ranging from 0.29 to 0.44 eV in the ordered x = 2.667, 4 structures. Li diffusion at higher levels of lithiation occurs via a vacancy-based mechanism, and so the diffusivity observed experimentally will be sensitive to the concentration of vacancies on different square-planar and square-pyramidal sites in the structure. The barriers for cross-block diffusion were found to be considerably higher, from 0.85 to 0.9 eV, suggesting that cross-block diffusion does not play a significant role at high or low levels of lithiation. While we examined some key Li compositions—(i) dilute, (ii) near the end of the second discharge region, and (iii) Li stuffed—a more in-depth analysis of the change in the Li hopping barriers as a function of Li content is an important topic and could also be approached with a more intensive cluster expansion based methodology,[65] although this is beyond the scope of the current work.

Behavior of "Beyond-Li" Cations. To test how the nature of the cation affects the motional activation barrier, the Li^+ ion in the transition state configurations associated with *b* axis diffusion (configurations *i* and *ii*) of the ordered $TiNb_2O_7$ supercell was replaced with a Na^+, K^+, or Mg^{2+} ion. The corresponding activation barriers were then found with HEF approach, as shown in Figure 11. For all of the beyond-Li cations, the barriers for *b* axis diffusion along tunnel T1 or tunnel T2 are considerably larger than the corresponding Li barriers with $\Delta E_{Li^+} \ll \Delta E_{Mg^{2+}} < \Delta E_{Na^+} \ll \Delta E_{K^+}$. For the Na^+

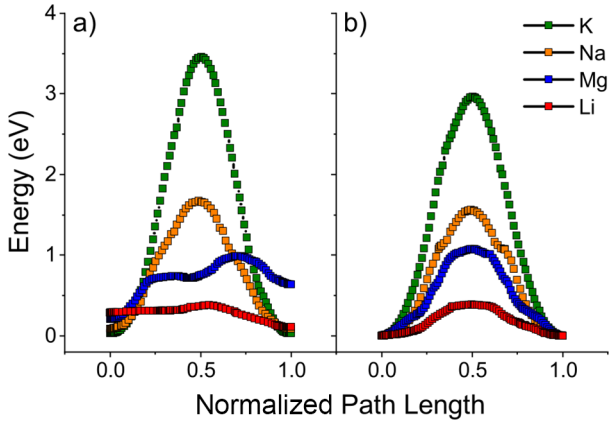

Figure 11. *b* axis diffusion mechanisms of Li^+, Na^+, K^+, and Mg^{2+} in the ordered supercell structure of $TiNb_2O_7$ initiated from (a) configuration *i* in tunnel T2 and (b) configuration *ii* in tunnel T1 (Figure 8a). The energies for each system are scaled relative to the lowest energy minimum in (b).

DOI: 10.1021/jacs.9b06669
J. Am. Chem. Soc. 2019, 141, 16706–16725

and K^+ systems, the minima in both tunnels in Figure 11 occur when the Na^+/K^+ ion occupies the 12-coordinate site at the center of the tunnel. In both tunnels, the transition state occurs when Na^+/K^+ passes through the square-planar configuration, which corresponds to minimum Li_A (tunnel 2) and transition state configuration *ii* (tunnel T1), in the Li system. The increase in the activation barrier along the series Li → Na → K can be related to the increase in the ionic radius 0.76 → 1.02 → 1.38 Å, respectively, which leads to increased repulsion as the A^+ ion passes through the square-planar AO_4 transition state.

For the Mg^{2+} system, the minimum in tunnel T1 (Figure 11b) corresponds to the distorted-square-pyramidal site analogous to position Li_C and the transition state corresponds to the square-planar position analogous to configuration *ii*. From Bader charge analysis,[98,99] the charge on the Mg ion in configuration *ii* was +1.75 e^-, consistent with the full ionization of Mg to Mg^{2+}. In tunnel T2 (Figure 11a), two local minima were found for Mg^{2+}: a square-pyramidal site (0.2 eV), analogous to position Li_B, and a highly distorted square planar site (0.64 eV), analogous to Li_A. Although the positions of the local minima are the same between the Li and Mg systems, the higher charge in the latter case results in an increase in the electrostatic repulsion at the transition state and thus a higher activation barrier (~1 eV). Although only a selected number of pathways were investigated for Na^+, K^+, and Mg^{2+}, these results suggest that the diffusion barriers for these ions are intrinsically much larger than for Li^+, which explains the requirement for nanosizing in the Na^+ system.[53−56]

DISCUSSION

Implications of Electronic Conductivity. Battery electrodes are mixed ionic−electronic conductors; therefore, low electrical resistivity is required, especially for operation at high current densities. Thus, $TiNb_2O_7$ might not be an obvious choice for a high-rate electrode material from e.g. band structure screening for small-band-gap materials, as it is a white, wide-band-gap insulator with a measured optical band gap of 3.06(2) eV (Figure S9 in the Supporting Information). Indeed, the experimental resistivity of a sintered pellet of $TiNb_2O_7$ is estimated from Xing et al.[82] to be ~10^9 Ω cm at room temperature, by Arrhenius extrapolation from higher-temperature measurements. However, $TiNb_2O_7$ does show good rate performance, indicating that this picture is incomplete because it does not account for the step-change increase in electronic conductivity upon lithiation. It is a general feature of shear structures that their conductive properties make it possible to lithiate, at least up to one Li/TM, pure polycrystalline pellets without the need for conductive additives or binder; this enables a variety of intrinsic measurements as a function of lithium content with relatively high precision.[21,23,34]

Due to the low conductivity of pristine $TiNb_2O_7$, many studies have focused on improving the this parameter via transition-metal doping,[29,100] partial reduction under a low oxygen partial pressure,[101] or partial nitridation.[38] Furthermore, these strategies are also being applied to related shear structures.[102−106] In light of the changes in resistivity as a function of lithiation, this approach should be reevaluated: while those methods do improve the transport by decades vs the insulating host, lithium intercalation has the same effect. For battery electrodes, which vary significantly in composition and often exhibit large changes in properties during operation, it is important to consider the full compositional range, not only the host structure and/or end point.

Crystallographic Shear Structure: Electronic/Ionic Property Relationships. Analogies can be drawn between ternary $TiNb_2O_7$ upon reduction by lithium and the crystallographic shear structures of binary $Nb_2O_{5-\delta}$, which are reduced by oxygen deficiency. Cava et al.[107−109] studied the magnetism of these latter phases and found effective magnetic moments—normalized to the number of d^1 electrons ($\mu_{eff}^{e^-}$)—of 1.18, 1.17, 1.39, and 1.14 for $Nb_{25}O_{62}$, $Nb_{47}O_{116}$, $Nb_{22}O_{54}$, and both orthorhombic and monoclinic (*o*,*m*)-$Nb_{12}O_{29}$, respectively. The magnitude of $\mu_{eff}^{e^-}$ for both $Li_{0.30}TiNb_2O_7$ and $Li_{0.60}TiNb_2O_7$ is 1.09, corresponding to localization of only 43% of the electron density if we take both Nb^{4+} and Ti^{3+} to be d^1, $S = 1/2$, $g = 2$. All of these $Nb_2O_{5-\delta}$ shear structures exhibit low resistivity at room temperature ($\rho = 3 \times 10^{-1}$ to 4×10^{-3} Ω cm) and behave as metals or heavily doped semiconductors.[107] Furthermore, *m*-$Nb_{12}O_{29}$ was shown to simultaneously display metallic conductivity and local moment magnetism with low-temperature antiferromagnetic ordering.[109,110] This intriguing behavior has been assigned to two subsets of the structure and the electron character—an itinerant electron within the crystallographic shear planes, which conducts along the *b* axis,[111] and a localized electron within the ReO_3-like block.[69] If one electron per formula unit is assumed to be itinerant and one assumed to be localized in $Nb_{12}O_{29}$, the one-electron $\mu_{eff}^{e^-}$ value becomes 1.61, in agreement with expectations for this $4d^1$ configuration.[107]

In a systematic single-crystal study, Rüscher convincingly demonstrated that $Nb_2O_{5-\delta}$ shear structures exhibit metallic behavior along the *b* axis, i.e. down the tunnels, and insulator-like properties in the *ac* plane perpendicular to the tunnels,[111] consistent with electronic band structure calculations of niobium suboxides.[69] Crystal structure analysis of $TiNb_2O_7$ and niobia crystallographic shear phases shows significantly shorter metal−metal interatomic distances via edge-shared octahedra along the shear planes (3.2−3.4 Å) in comparison to the *ac* planar cross-block metal−metal pathways (≥3.8 Å). In contrast to the perovskite structure with 180° −M−O−M− orbital interactions, the edge-sharing planes of the crystallographic shear structures provide electric "wires" running parallel to the columns. This suggests that long-range electronic conduction is down the *b* axis in $TiNb_2O_7$ and the other shear oxides,[69] which is also the direction of long-range ionic conduction.

Altogether, comparisons of the magnetic and electronic behavior of $TiNb_2O_7$ with $Nb_2O_{5-\delta}$ crystallographic shear structures suggest that the hierarchical crystal structure comprising shear planes and block motifs may enable some degree of room-temperature electron delocalization as well as the observed local moments. The partially localized, partially delocalized electronic behavior may explain the large increase in conductivity due to lithium insertion in $TiNb_2O_7$, even at low doping levels and in the presence of Curie−Weiss paramagnetism. Meanwhile, $TiNb_2O_7$ differs from $Nb_2O_{5-\delta}$ due to the presence of Ti and of cation mixing. One effect of this, elucidated from the DFT calculations, is that the electron localization in $TiNb_2O_7$ is associated with Ti atoms; Ti atoms, though disordered, preferentially occupy shear plane sites so that spin density is observed at block edges in $TiNb_2O_7$ vs block centers in $Nb_2O_{5-\delta}$.[69] The localized state roughly 1 eV

DOI: 10.1021/jacs.9b06669
J. Am. Chem. Soc. 2019, 141, 16706−16725

within the band gap of $TiNb_2O_7$ (Figure 4) is consistent with the electronic localization in n-type TiO_2[112] and suggests that the electronic localization in 3*d* Ti-containing crystallographic shear phases is stronger than in 4*d* niobium oxides or 4*d*−5*d* niobium tungsten oxides with larger *d* orbitals, which has implications for the electronic conductivity.

The cation disorder also has implications for the ionic conductivity upon lithiation. Four- and five-coordinate Li sites can be either ground states or transition states depending on the tunnel and cation configuration. Additionally, metal cation disorder creates local structural effects such as split Li sites with very small intrasite hopping barriers. The small blocks of $TiNb_2O_7$ (3 × 3) require that every tunnel straddles shear planes and central corner-shared octahedra. An interesting future direction will be to examine the different ionic transport properties through central tunnels vs edge tunnels in crystallographic shear structures with larger block sizes, on top of the role of cation disorder.

High-Temperature NMR Spectroscopy. For a fast ion conductor at room temperature, motional narrowing of NMR line shapes is expected, but in the case of crystallographic shear titanium niobium oxide, it might appear that only limited line narrowing is observed from 295 to ca. 1000 K. There are significant changes to the spinning sideband manifold from the satellite transitions at high temperatures and resolved peaks do appear within the central transition. The high-temperature line shapes are neither pseudo-Voigt nor quadrupolar. However, a fit to the whole pattern can be obtained by the combination of a series of shift-distributed narrow pseudo-Voigt lines (Figure 12). Individual peaks have a fwhm of ca. 80 Hz (0.5 ppm) with the edges of the line shape constraining the maximum line width of the components. The obtained fit was produced with the shift and quadrupolar tensor parameters in Table 2. The unusual central and sideband peak distribution is observed in all spectra with the exception of $Li_{0.75}TiNb_2O_7$; the peaks emerging within the central transition resonance and sidebands are most prominent at low lithiation. Strikingly similar line shapes were observed in the ^{19}F NMR spectra of a niobium fluoride due to $^1J(^{19}F,^{93}Nb)$ indirect coupling to the $I = 9/2$ ^{93}Nb nucleus ($2I + 1 = 10$) with partial motional averaging of the dipolar coupling under MAS-induced or VT heating.[113] We would expect the $^2J(^7Li,^{93}Nb)$ coupling to be weaker. This is also consistent; a $^1J(^{19}F,^{93}Nb)$ value of 204(2) Hz was found in the former case, and a $^2J(^7Li,^{93}Nb)$ value of 90(10) Hz would be consistent with the spectra presented here. Increased residual dipolar coupling is expected in the lithium-rich compositions, remaining even under MAS at high temperatures, due to the persistence of homonuclear $^7Li-^7Li$ dipolar coupling[47,89,114] relative to heteronuclear $^7Li-^{93}Nb$ dipolar coupling. Alternatively, it is possible that this effect could arise from residual dipolar[115] or *J*[116] coupling between quadrupolar nuclei in the presence of anisotropic motion.

Lithium Diffusion. On comparison of the DFT-computed conduction barriers with the activation energies from NMR, for dilute Li contents, the small energies from NMR within the low-temperature regime (0.020−0.085 eV) can be tentatively assigned to the rapid Li exchange between split sites within the same ReO_3-like cage. At high states of lithiation, the DFT calculations show a transition from an interstitial to a vacancy diffusion mechanism, which eliminates rattling between split sites within the blocks. NMR measurements on highly lithiated samples do not show these ultralow barrier processes, consistent with the DFT results. The activation energies (0.060−0.390 eV) from NMR at higher temperatures can then be tentatively assigned to a combination of Li diffusion along the *b* axis (configurations *i* and *ii*), aided by facile hopping between tunnels T1 and T2 (configurations *iii* and *iv*) and diffusion between square-pyramidal sites on the edges of the tunnel (configuration *v*), primarily Li_D sites. The large activation barriers between blocks (configurations *ix*−*xi*) for all local Ti/Nb orderings suggests that the diffusion mechanism in Li-doped $TiNb_2O_7$ is primarily 1D in nature. The situation is analogous to the rapid down-tunnel diffusion but high cross-tunnel energies in $LiFePO_4$[117] and TiO_2(B),[95] the important difference in $TiNb_2O_7$ and other crystallographic

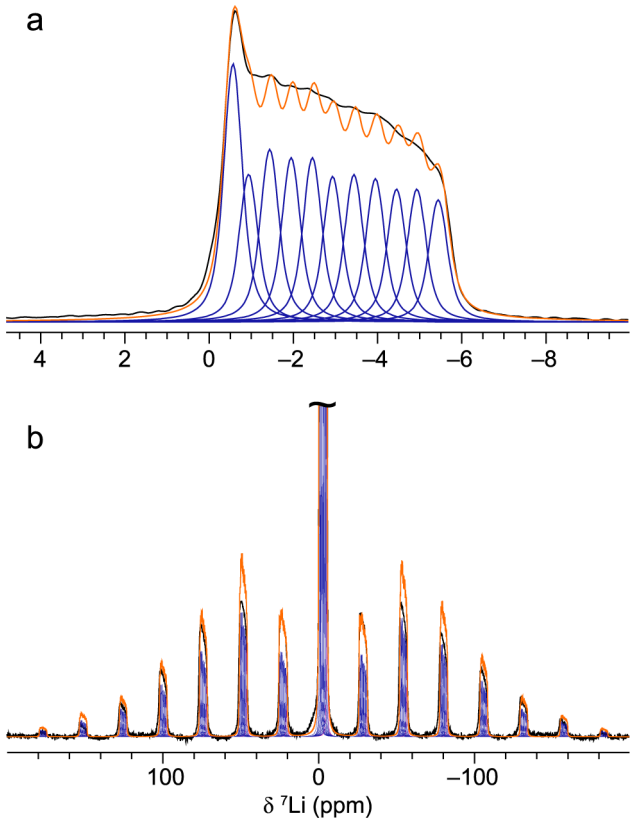

Figure 12. ^7Li MAS NMR spectrum of $Li_{0.30}TiNb_2O_7$ at ca. 670 K. The unique line shapes of the (a) central transition and (b) spinning sideband manifold were fit as described in the text. The spectrum was recorded at 4 kHz MAS and 9.4 T. Fitting parameters are given in Table 2. Experimental data are given in black, individual fit components are given in blue, and the sum of the fit is given in orange. This is not necessarily a unique or an optimized fit but rather a reproduction of the observed spectrum with minimum variables.

Table 2. NMR Shift and Quadrupolar Tensors Fit to the ^7Li NMR Spectrum of $Li_{0.30}TiNb_2O_7$ at ca. 670 K[a]

param	site 1	sites 2−11
$\delta(^7Li)$ (ppm)	−0.5	site (N − 1) + 0.5
CSA (ppm)	10 (10)	10 (10)
η_{CSA}	0	0
C_Q (kHz)	12 (2)	55 (5)
η_Q	0	0

[a]*N* indicates the site number. η values were set to zero and not refined. The fits were also not very sensitive to CSA for values below 20 ppm. Line broadening of 100 Hz was used for each site (1:1 Gaussian:Lorentzian line shape).

DOI: 10.1021/jacs.9b06669
J. Am. Chem. Soc. 2019, 141, 16706−16725

shear structures[23] being the multiple parallel tunnels with low intrablock hopping energies between tunnels.

High-Rate Energy Storage. Among crystallographic shear structures for lithium ion batteries, the gravimetric capacity of $TiNb_2O_7$ is one of the highest at lower C rates but drops precipitously at higher rates even at the low mass loadings used here, due in part to the rapid increase in E_a as lithiation approaches 1 Li/TM. In $TiNb_2O_7$, the dQ/dV peak width measured for the discharge process is always broader than that of the charge process (Figure 2b), indicating a more kinetically hindered process for lithium insertion than for lithium extraction. This behavior is atypical for crystallographic shear structures. Although dQ/dV curves are not widely reported as a function of rate, there is no evidence for this noticeable lithiation−delithiation asymmetry in $Nb_{12}WO_{33}$,[118,119] $Nb_{16}W_5O_{55}$,[23] $TiNb_{24}O_{62}$,[33] or H-Nb_2O_5.[21] A kinetic limitation on discharge in a half-cell is in agreement with numerous reports that lithiation is the rate-limiting step for $TiNb_2O_7$.[26,28,30,120] In a full cell configuration, $TiNb_2O_7$ is the negative electrode and lithium insertion occurs on charging; the implication is that the full cell charging rate could be lower than the discharge rate: i.e., high power output but comparatively slower charging. The niobium tungsten oxides, even at higher mass loadings, show higher gravimetric capacity and symmetric lithiation/delithiation voltage curves at high C rates while having 20−30% higher density.[23] Among the emerging complex oxide anode materials, further electrode engineering and electrochemical testing is required to determine the crossing points in the tradeoffs between gravimetric vs volumetric capacity and low-to-intermediate rate performance vs high rate performance. The demands of the application will ultimately determine the optimal material selection.

While lithium experiences low activation barriers to move through the crystallographic shear structure of $TiNb_2O_7$, larger alkali cations and divalent cations are considerably more hindered. This compound may not be suitable for "beyond lithium" rechargeable batteries, but a related phase with similar structural motifs and larger tunnels may enable intercalation of alternative species.

CONCLUSION

Via experiment, theory, and comparisons to related crystallographic shear structures, we conclude that ionic and electronic conduction are strongly anisotropic in $TiNb_2O_7$ to the extent that they can be approximated as one-dimensional in the direction along the tunnel (b axis). The anisotropy in both Li^+ and e^- conduction arises due to the crystallographic shear planes that disrupt transport in the ac plane. Nevertheless, the bulk structure is capable of high-rate (de)lithiation. The ReO_3-like blocks of octahedra in this complex oxide allow facile Li diffusion characterized by activation barriers of <100 meV from variable-temperature NMR, at lithium concentrations below one lithium per transition metal ($Li_3TiNb_2O_7$), and 100−200 meV from single-ended transition state searching calculations. Lithium diffusivity decreases rapidly at and above one-electron redox capacities, as evidenced by high-temperature ^{7}Li NMR (E_a = 300−400 meV), $^{6/7}$Li NMR spectral line widths, and GITT measurements, which explains the lower lithium storage capacities at higher rates. The crystallographic shear planes, while essentially prohibiting Li^+ diffusion perpendicular to the tunnels, hold the framework open and provide structural stability. Electronically, n-type doping of $TiNb_2O_7$ by the addition of Li atoms ($Li^0 = Li^+ + e^-$) increases the electronic conductivity of the host by ca. seven orders of magnitude even at low doping concentrations. At low lithium concentrations, localized paramagnetism is observed via measurements of the magnetic susceptibility and $^{6/7}$Li NMR spectroscopy, though the magnetic moment is smaller than expected. This result suggests the possibility of the simultaneous presence of localized and delocalized electrons. At higher lithium concentrations, NMR and magnetic susceptibility measurements suggest that the system becomes metallic. Li can occupy a range of four- and five-coordinate sites within the ReO_3 blocks, and the energies of the local minima and transition states are subtly related to the presence of the Ti/Nb local ordering. The availability of multiple adjacent Li minima with similar energies is a crucial factor that leads to the facile conduction in the $TiNb_2O_7$ structure. At high lithium concentrations, the activation barriers for intersite Li hopping are relatively unchanged in comparison to the dilute limit. However, the diffusion mechanism transitions from interstitial-mediated to vacancy-mediated and the vacancy formation energetics—specifically for inner block sites that lead to long-range Li^+ diffusion—may become rate-determining. With the framework established for Li ground-state and transition-state searching, the diffusion of intercalant species Na^+, K^+, and Mg^{2+} was examined. These cations all exhibit very high diffusion barriers of at least ca. 1.0 eV, suggesting minimal conduction at room temperature.

ASSOCIATED CONTENT

Supporting Information

The Supporting Information is available free of charge on the ACS Publications website at DOI: 10.1021/jacs.9b06669.

Supplementary methods; structural characterization; additional electrochemical measurements, including GITT, magnetic, electrical, and optical property curves; additional lithium NMR spectra with a range of compositions, temperatures, and effects of an echo pulse sequence; bond valence sum map of $TiNb_2O_7$; additional kinetic barrier figures at dilute and concentrated Li contents for ordered and disordered Ti/Nb configurations; and calculated local structures and NMR parameters. Data supporting this work are available at www.repository.cam.ac.uk. (PDF)

Movie of lithium hopping pathway from site A, through transition state *i*, to site B (MPG)

Movie of lithium hopping pathway from site B, through transition state *iii*, to site C (MPG)

Movie of lithium hopping pathway from site B, through transition state *vii*, to site F (MPG)

Movie of lithium hopping pathway from site B, through transition state *viii*, to site G (MPG)

Movie of lithium hopping pathway from site C, through transition state *ii*, to site C (MPG)

Movie of lithium hopping pathway from site C, through transition state *iv*, to site B (MPG)

Movie of lithium hopping pathway from site C, through transition state *v*, to site D (MPG)

Movie of lithium hopping pathway from site E, through transition state *vi*, to site C (MPG)

Movie of lithium hopping pathway from site E, through transition state *x*, to site E (MPG)

DOI: 10.1021/jacs.9b06669
J. Am. Chem. Soc. 2019, 141, 16706−16725

Movie of lithium hopping pathway from site F, through transition state *ix*, to site D (MPG)
Movie of lithium hopping pathway from site G, through transition state *xi*, to site G (MPG)

AUTHOR INFORMATION

Corresponding Author

*E-mail for C.P.G.: cpg27@cam.ac.uk.

ORCID

Kent J. Griffith: 0000-0002-8096-906X
Michael A. Hope: 0000-0002-4742-9336
Megan M. Butala: 0000-0002-7759-5300
Molleigh B. Preefer: 0000-0002-3699-8613
Can P. Koçer: 0000-0003-0477-5148
Graeme Henkelman: 0000-0002-0336-7153
Andrew J. Morris: 0000-0001-7453-5698
Matthew J. Cliffe: 0000-0002-0408-7647
Siân E. Dutton: 0000-0003-0984-5504
Clare P. Grey: 0000-0001-5572-192X

Author Contributions

#K.J.G. and I.D.S. contributed equally.

Notes

The authors declare the following competing financial interest(s): K.J.G. and C.P.G. are major shareholders in a start-up company developing fast-charging batteries based on high-rate anode materials.

ACKNOWLEDGMENTS

K.J.G. thanks the Winston Churchill Foundation of the United States, the Herchel Smith Scholarship, and the EPSRC (EP/M009521/1) for funding. M.A.H. acknowledges support from the Oppenheimer Foundation. A.J.M. acknowledges support from the EPSRC (EP/P003532/1). Via our membership of the UK's HEC Materials Chemistry Consortium, which is funded by EPSRC (EP/L000202, EP/R029431), this work used the ARCHER UK National Computing Service. M.J.C. thanks Sidney Sussex College, University of Cambridge, for financial support. K.J.G. thanks Dr. John Griffin, University of Lancaster, for discussions of homonuclear and heteronuclear dipolar coupling; Professor Ram Seshadri, University of California, Santa Barbara, for experimental advice; and Charles Creissen, University of Cambridge, for assistance with diffuse reflectance spectroscopy. I.D.S. thanks Professor David J. Wales and Dr. Roberta Pigliapochi, University of Cambridge, for discussions on transition-state energetics. S.E.D. and C.P.K. acknowledge funding from the Winton Programme for the Physics of Sustainability. Magnetic measurements were carried out on the Advanced Materials Characterisation Suite funded by EPSRC Strategic Equipment Grant EP/M000524/1.

REFERENCES

(1) *X-CELL: EXtreme Fast Charge Cell Evaluation of Lithium-Ion Batteries*; Argonne National Laboratory/Idaho National Laboratory/National Renewable Energy Laboratory, 2018; p 29.

(2) Zhang, S. S.; Xu, K.; Jow, T. R. Study of the Charging Process of a $LiCoO_2$-Based Li-Ion Battery. *J. Power Sources* **2006**, *160* (2), 1349−1354.

(3) Zhao, K.; Pharr, M.; Vlassak, J. J.; Suo, Z. Fracture of Electrodes in Lithium-Ion Batteries Caused by Fast Charging. *J. Appl. Phys.* **2010**, *108* (7), No. 073517.

(4) Lu, W.; López, C. M.; Liu, N.; Vaughey, J. T.; Jansen, A.; Dees, D. W. Overcharge Effect on Morphology and Structure of Carbon Electrodes for Lithium-Ion Batteries. *J. Electrochem. Soc.* **2012**, *159* (5), A566−A570.

(5) Burns, J. C.; Stevens, D. A.; Dahn, J. R. In-Situ Detection of Lithium Plating Using High Precision Coulometry. *J. Electrochem. Soc.* **2015**, *162* (6), A959−A964.

(6) Cannarella, J.; Arnold, C. B. The Effects of Defects on Localized Plating in Lithium-Ion Batteries. *J. Electrochem. Soc.* **2015**, *162* (7), A1365−A1373.

(7) Lin, D.; Liu, Y.; Cui, Y. Reviving the Lithium Metal Anode for High-Energy Batteries. *Nat. Nanotechnol.* **2017**, *12* (3), 194−206.

(8) Bhattacharyya, R.; Key, B.; Chen, H.; Best, A. S.; Hollenkamp, A. F.; Grey, C. P. In Situ NMR Observation of the Formation of Metallic Lithium Microstructures in Lithium Batteries. *Nat. Mater.* **2010**, *9* (6), 504−510.

(9) Wandt, J.; Marino, C.; Gasteiger, H. A.; Jakes, P.; Eichel, R.-A.; Granwehr, J. Operando Electron Paramagnetic Resonance Spectroscopy − Formation of Mossy Lithium on Lithium Anodes during Charge−Discharge Cycling. *Energy Environ. Sci.* **2015**, *8* (4), 1358−1367.

(10) Cheng, J.-H.; Assegie, A. A.; Huang, C.-J.; Lin, M.-H.; Tripathi, A. M.; Wang, C.-C.; Tang, M.-T.; Song, Y.-F.; Su, W.-N.; Hwang, B. J. Visualization of Lithium Plating and Stripping via in Operando Transmission X-Ray Microscopy. *J. Phys. Chem. C* **2017**, *121* (14), 7761−7766.

(11) Ribière, P.; Grugeon, S.; Morcrette, M.; Boyanov, S.; Laruelle, S.; Marlair, G. Investigation on the Fire-Induced Hazards of Li-Ion Battery Cells by Fire Calorimetry. *Energy Environ. Sci.* **2012**, *5* (1), 5271−5280.

(12) Finegan, D. P.; Scheel, M.; Robinson, J. B.; Tjaden, B.; Hunt, I.; Mason, T. J.; Millichamp, J.; Michiel, M. D.; Offer, G. J.; Hinds, G.; Brett, D. J. L.; Shearing, P. R. In-Operando High-Speed Tomography of Lithium-Ion Batteries during Thermal Runaway. *Nat. Commun.* **2015**, *6*, 6924.

(13) Brownson, E. G.; Thompson, C. M.; Goldsberry, S.; Chong, H. J.; Friedrich, J. B.; Pham, T. N.; Arbabi, S.; Carrougher, G. J.; Gibran, N. S. Explosion Injuries from E-Cigarettes. *N. Engl. J. Med.* **2016**, *375* (14), 1400−1402.

(14) Finegan, D. P.; Darcy, E.; Keyser, M.; Tjaden, B.; Heenan, T. M. M.; Jervis, R.; Bailey, J. J.; Malik, R.; Vo, N. T.; Magdysyuk, O. V.; Atwood, R.; Drakopoulos, M.; DiMichiel, M.; Rack, A.; Hinds, G.; Brett, D. J. L.; Shearing, P. R. Characterising Thermal Runaway within Lithium-Ion Cells by Inducing and Monitoring Internal Short Circuits. *Energy Environ. Sci.* **2017**, *10* (6), 1377−1388.

(15) Armstrong, A. R.; Armstrong, G.; Canales, J.; Bruce, P. G. TiO_2-B Nanowires. *Angew. Chem., Int. Ed.* **2004**, *43* (17), 2286−2288.

(16) Beuvier, T.; Richard-Plouet, M.; Mancini-Le Granvalet, M.; Brousse, T.; Crosnier, O.; Brohan, L. TiO_2(B) Nanoribbons As Negative Electrode Material for Lithium Ion Batteries with High Rate Performance. *Inorg. Chem.* **2010**, *49* (18), 8457−8464.

(17) Ren, Y.; Liu, Z.; Pourpoint, F.; Armstrong, A. R.; Grey, C. P.; Bruce, P. G. Nanoparticulate TiO_2(B): An Anode for Lithium-Ion Batteries. *Angew. Chem., Int. Ed.* **2012**, *51* (9), 2164−2167.

(18) Billet, J.; Dujardin, W.; De Keukeleere, K.; De Buysser, K.; De Roo, J.; Van Driessche, I. Size Tunable Synthesis and Surface Chemistry of Metastable TiO_2-Bronze Nanocrystals. *Chem. Mater.* **2018**, *30* (13), 4298−4306.

(19) Augustyn, V.; Come, J.; Lowe, M. A.; Kim, J. W.; Taberna, P.-L.; Tolbert, S. H.; Abruña, H. D.; Simon, P.; Dunn, B. High-Rate Electrochemical Energy Storage through Li^+ Intercalation Pseudocapacitance. *Nat. Mater.* **2013**, *12* (6), 518−522.

(20) Come, J.; Augustyn, V.; Kim, J. W.; Rozier, P.; Taberna, P.-L.; Gogotsi, P.; Long, J. W.; Dunn, B.; Simon, P. Electrochemical Kinetics of Nanostructured Nb_2O_5 Electrodes. *J. Electrochem. Soc.* **2014**, *161* (5), A718−A725.

(21) Griffith, K. J.; Forse, A. C.; Griffin, J. M.; Grey, C. P. High-Rate Intercalation without Nanostructuring in Metastable Nb_2O_5 Bronze Phases. *J. Am. Chem. Soc.* **2016**, *138* (28), 8888−8899.

(22) Sun, H.; Mei, L.; Liang, J.; Zhao, Z.; Lee, C.; Fei, H.; Ding, M.; Lau, J.; Li, M.; Wang, C.; Xu, X.; Hao, G.; Papandrea, B.; Shakir, I.;

DOI: 10.1021/jacs.9b06669
J. Am. Chem. Soc. 2019, 141, 16706−16725

Dunn, B.; Huang, Y.; Duan, X. Three-Dimensional Holey-Graphene/Niobia Composite Architectures for Ultrahigh-Rate Energy Storage. *Science* **2017**, *356* (6338), 599−604.
(23) Griffith, K. J.; Wiaderek, K. M.; Cibin, G.; Marbella, L. E.; Grey, C. P. Niobium Tungsten Oxides for High-Rate Lithium-Ion Energy Storage. *Nature* **2018**, *559* (7715), 556−563.
(24) Han, J.-T.; Huang, Y.-H.; Goodenough, J. B. New Anode Framework for Rechargeable Lithium Batteries. *Chem. Mater.* **2011**, *23* (8), 2027−2029.
(25) Han, J.-T.; Goodenough, J. B. 3-V Full Cell Performance of Anode Framework $TiNb_2O_7$/Spinel $LiNi_{0.5}Mn_{1.5}O_4$. *Chem. Mater.* **2011**, *23* (15), 3404−3407.
(26) Tang, K.; Mu, X.; van Aken, P. A.; Yu, Y.; Maier, J. Nano-Pearl-String" $TiNb_2O_7$ as Anodes for Rechargeable Lithium Batteries. *Adv. Energy Mater.* **2013**, *3* (1), 49−53.
(27) Li, H.; Shen, L.; Pang, G.; Fang, S.; Luo, H.; Yang, K.; Zhang, X. $TiNb_2O_7$ Nanoparticles Assembled into Hierarchical Microspheres as High-Rate Capability and Long-Cycle-Life Anode Materials for Lithium Ion Batteries. *Nanoscale* **2015**, *7* (2), 619−624.
(28) Guo, B.; Yu, X.; Sun, X.-G.; Chi, M.; Qiao, Z.-A.; Liu, J.; Hu, Y.-S.; Yang, X.-Q.; Goodenough, J. B.; Dai, S. A Long-Life Lithium-Ion Battery with a Highly Porous $TiNb_2O_7$ Anode for Large-Scale Electrical Energy Storage. *Energy Environ. Sci.* **2014**, *7* (7), 2220−2226.
(29) Song, H.; Kim, Y.-T. A Mo-Doped $TiNb_2O_7$ Anode for Lithium-Ion Batteries with High Rate Capability Due to Charge Redistribution. *Chem. Commun.* **2015**, *51* (48), 9849−9852.
(30) Cheng, Q.; Liang, J.; Lin, N.; Guo, C.; Zhu, Y.; Qian, Y. Porous $TiNb_2O_7$ Nanospheres as Ultra Long-Life and High-Power Anodes for Lithium-Ion Batteries. *Electrochim. Acta* **2015**, *176*, 456−462.
(31) Takami, N.; Ise, K.; Harada, Y.; Iwasaki, T.; Kishi, T.; Hoshina, K. High-Energy, Fast-Charging, Long-Life Lithium-Ion Batteries Using $TiNb_2O_7$ Anodes for Automotive Applications. *J. Power Sources* **2018**, *396*, 429−436.
(32) Roth, R. S. Thermal Stability of Long Range Order in Oxides. *Prog. Solid State Chem.* **1980**, *13* (2), 159−192.
(33) Griffith, K. J.; Senyshyn, A.; Grey, C. P. Structural Stability from Crystallographic Shear in TiO_2−Nb_2O_5 Phases: Cation Ordering and Lithiation Behavior of $TiNb_{24}O_{62}$. *Inorg. Chem.* **2017**, *56* (7), 4002−4010.
(34) Lu, X.; Jian, Z.; Fang, Z.; Gu, L.; Hu, Y.-S.; Chen, W.; Wang, Z.; Chen, L. Atomic-Scale Investigation on Lithium Storage Mechanism in $TiNb_2O_7$. *Energy Environ. Sci.* **2011**, *4* (8), 2638−2644.
(35) Catti, M.; Pinus, I.; Knight, K. Lithium Insertion Properties of $Li_xTiNb_2O_7$ Investigated by Neutron Diffraction and First-Principles Modelling. *J. Solid State Chem.* **2015**, *229*, 19−25.
(36) Hu, L.; Lin, C.; Wang, C.; Yang, C.; Li, J.; Chen, Y.; Lin, S. $TiNb_2O_7$ Nanorods as a Novel Anode Material for Secondary Lithium-Ion Batteries. *Funct. Mater. Lett.* **2016**, *09* (06), 1642004.
(37) Lou, S.; Ma, Y.; Cheng, X.; Gao, J.; Gao, Y.; Zuo, P.; Du, C.; Yin, G. Facile Synthesis of Nanostructured $TiNb_2O_7$ Anode Materials with Superior Performance for High-Rate Lithium Ion Batteries. *Chem. Commun.* **2015**, *51*, 17293−17296.
(38) Park, H.; Wu, H. B.; Song, T.; David Lou, X. W.; Paik, U. Porosity-Controlled $TiNb_2O_7$ Microspheres with Partial Nitridation as A Practical Negative Electrode for High-Power Lithium-Ion Batteries. *Adv. Energy Mater.* **2015**, *5* (8), 1401945.
(39) Wang, X.; Shen, G. Intercalation Pseudo-Capacitive $TiNb_2O_7$@carbon Electrode for High-Performance Lithium Ion Hybrid Electrochemical Supercapacitors with Ultrahigh Energy Density. *Nano Energy* **2015**, *15*, 104−115.
(40) Yoon, S.; Lee, S.-Y.; Nguyen, T. L.; Kim, I. T.; Woo, S.-G.; Cho, K. Y. Controlled Synthesis of Dual-Phase Carbon-Coated Nb_2O_5/$TiNb_2O_7$ Porous Spheres and Their Li-Ion Storage Properties. *J. Alloys Compd.* **2018**, *731*, 437−443.
(41) Buannic, L.; Colin, J.-F.; Chapuis, M.; Chakir, M.; Patoux, S. Electrochemical Performances and Gassing Behavior of High Surface Area Titanium Niobium Oxides. *J. Mater. Chem. A* **2016**, *4* (29), 11531−11541.
(42) Palacin, M. R.; Simon, P.; Tarascon, J. M. Nanomaterials for Electrochemical Energy Storage: The Good and the Bad. *Acta Chim. Slov.* **2016**, *63*, 417−423.
(43) Trease, N. M.; Zhou, L.; Chang, H. J.; Zhu, B. Y.; Grey, C. P. In Situ NMR of Lithium Ion Batteries: Bulk Susceptibility Effects and Practical Considerations. *Solid State Nucl. Magn. Reson.* **2012**, *42*, 62−70.
(44) Pecher, O.; Carretero-González, J.; Griffith, K. J.; Grey, C. P. Materials' Methods: NMR in Battery Research. *Chem. Mater.* **2017**, *29* (1), 213−242.
(45) Vinod Chandran, C.; Heitjans, P.; Webb, G. A. Solid-State NMR Studies of Lithium Ion Dynamics Across Materials Classes. *Annu. Rep. NMR Spectrosc.* **2016**, *89*, 1−102.
(46) Kuhn, A.; Sreeraj, P.; Pöttgen, R.; Wiemhöfer, H.-D.; Wilkening, M.; Heitjans, P. Li Ion Diffusion in the Anode Material $Li_{12}Si_7$: Ultrafast Quasi-1D Diffusion and Two Distinct Fast 3D Jump Processes Separately Revealed by ^{7}Li NMR Relaxometry. *J. Am. Chem. Soc.* **2011**, *133* (29), 11018−11021.
(47) Dunstan, M. T.; Griffin, J. M.; Blanc, F.; Leskes, M.; Grey, C. P. Ion Dynamics in Li_2CO_3 Studied by Solid-State NMR and First-Principles Calculations. *J. Phys. Chem. C* **2015**, *119* (43), 24255−24264.
(48) Bloembergen, N.; Purcell, E. M.; Pound, R. V. Relaxation Effects in Nuclear Magnetic Resonance Absorption. *Phys. Rev.* **1948**, *73* (7), 679−712.
(49) Kumeda, Y.; Munro, L.; Wales, D. J. Transition States and Rearrangement Mechanisms from Hybrid Eigenvector-Following and Density Functional Theory. Application to $C_{10}H_{10}$ and Defect Migration in Crystalline Silicon. *Chem. Phys. Lett.* **2001**, *341* (1), 185−194.
(50) Mills, G.; Jónsson, H. Quantum and Thermal Effects in H_2 Dissociative Adsorption: Evaluation of Free Energy Barriers in Multidimensional Quantum Systems. *Phys. Rev. Lett.* **1994**, *72* (7), 1124−1127.
(51) Mills, G.; Jónsson, H.; Schenter, G. K. Reversible Work Transition State Theory: Application to Dissociative Adsorption of Hydrogen. *Surf. Sci.* **1995**, *324* (2−3), 305−337.
(52) Ong, S. P.; Chevrier, V. L.; Hautier, G.; Jain, A.; Moore, C.; Kim, S.; Ma, X.; Ceder, G. Voltage, Stability and Diffusion Barrier Differences between Sodium-Ion and Lithium-Ion Intercalation Materials. *Energy Environ. Sci.* **2011**, *4* (9), 3680.
(53) Li, S.; Cao, X.; Schmidt, C. N.; Xu, Q.; Uchaker, E.; Pei, Y.; Cao, G. $TiNb_2O_7$/Graphene Composites as High-Rate Anode Materials for Lithium/Sodium Ion Batteries. *J. Mater. Chem. A* **2016**, *4* (11), 4242−4251.
(54) Huang, Y.; Li, X.; Luo, J.; Wang, K.; Zhang, Q.; Qiu, Y.; Sun, S.; Liu, S.; Han, J.; Huang, Y. Enhancing Sodium-Ion Storage Behaviors in $TiNb_2O_7$ by Mechanical Ball Milling. *ACS Appl. Mater. Interfaces* **2017**, *9* (10), 8696−8703.
(55) Shang, B.; Peng, Q.; Jiao, X.; Xi, G.; Hu, X. $TiNb_2O_7$/Carbon Nanotube Composites as Long Cycle Life Anode for Sodium-Ion Batteries. *Ionics* **2019**, *25*, 1679−1688.
(56) Deng, Q.; Fu, Y.; Zhu, C.; Yu, Y. Niobium-Based Oxides Toward Advanced Electrochemical Energy Storage: Recent Advances and Challenges. *Small* **2019**, *15*, 1804884.
(57) Rietveld, H. M. A Profile Refinement Method for Nuclear and Magnetic Structures. *J. Appl. Crystallogr.* **1969**, *2* (2), 65−71.
(58) Toby, B. H.; Von Dreele, R. B. GSAS-II: The Genesis of a Modern Open-Source All Purpose Crystallography Software Package. *J. Appl. Crystallogr.* **2013**, *46* (2), 544−549.
(59) Momma, K.; Izumi, F. VESTA 3 for Three-Dimensional Visualization of Crystal, Volumetric and Morphology Data. *J. Appl. Crystallogr.* **2011**, *44* (6), 1272−1276.
(60) Thurber, K. R.; Tycko, R. Measurement of Sample Temperatures under Magic-Angle Spinning from the Chemical Shift and Spin-Lattice Relaxation Rate of ^{79}Br in KBr Powder. *J. Magn. Reson.* **2009**, *196* (1), 84−87.
(61) Stone, N. J. Table of Nuclear Electric Quadrupole Moments. *At. Data Nucl. Data Tables* **2016**, *111-112*, 1−28.

DOI: 10.1021/jacs.9b06669
J. Am. Chem. Soc. 2019, 141, 16706−16725

(62) Perdew, J.; Burke, K.; Ernzerhof, M. Generalized Gradient Approximation Made Simple. *Phys. Rev. Lett.* **1996**, *77* (18), 3865−3868.
(63) Kresse, G.; Furthmüller, J. Efficient Iterative Schemes for Ab Initio Total-Energy Calculations Using a Plane-Wave Basis Set. *Phys. Rev. B: Condens. Matter Mater. Phys.* **1996**, *54* (16), 11169−11186.
(64) Blöchl, P. E. Projector Augmented-Wave Method. *Phys. Rev. B: Condens. Matter Mater. Phys.* **1994**, *50* (24), 17953−17979.
(65) Van der Ven, A.; Thomas, J. C.; Xu, Q.; Swoboda, B.; Morgan, D. Nondilute Diffusion from First Principles: Li Diffusion in Li_xTiS_2. *Phys. Rev. B: Condens. Matter Mater. Phys.* **2008**, *78* (10), 104306.
(66) Van der Ven, A.; Thomas, J. C.; Xu, Q.; Bhattacharya, J. Linking the Electronic Structure of Solids to Their Thermodynamic and Kinetic Properties. *Math. Comput. Simul.* **2010**, *80* (7), 1393−1410.
(67) Morgan, B. J.; Watson, G. W. Intrinsic N-Type Defect Formation in TiO_2: A Comparison of Rutile and Anatase from GGA +*U* Calculations. *J. Phys. Chem. C* **2010**, *114* (5), 2321−2328.
(68) Morgan, B. J.; Watson, G. W. GGA+*U* Description of Lithium Intercalation into Anatase TiO_2. *Phys. Rev. B: Condens. Matter Mater. Phys.* **2010**, *82* (14), 144119.
(69) Koçer, C. P.; Griffith, K. J.; Grey, C. P.; Morris, A. J. First-Principles Study of Localized and Delocalized Electronic States in Crystallographic Shear Phases of Niobium Oxide. *Phys. Rev. B: Condens. Matter Mater. Phys.* **2019**, *99* (7), 075151.
(70) Anisimov, V. I.; Zaanen, J.; Andersen, O. K. Band Theory and Mott Insulators: Hubbard *U* Instead of Stoner *I*. *Phys. Rev. B: Condens. Matter Mater. Phys.* **1991**, *44* (3), 943−954.
(71) Liechtenstein, A. I.; Anisimov, V. I.; Zaanen, J. Density-Functional Theory and Strong Interactions: Orbital Ordering in Mott-Hubbard Insulators. *Phys. Rev. B: Condens. Matter Mater. Phys.* **1995**, *52* (8), R5467−R5470.
(72) Nosé, S. A Unified Formulation of the Constant Temperature Molecular Dynamics Methods. *J. Chem. Phys.* **1984**, *81* (1), 511−519.
(73) Munro, L. J.; Wales, D. J. Defect Migration in Crystalline Silicon. *Phys. Rev. B: Condens. Matter Mater. Phys.* **1999**, *59* (6), 3969−3980.
(74) Seymour, I. D.; Chakraborty, S.; Middlemiss, D. S.; Wales, D. J.; Grey, C. P. Mapping Structural Changes in Electrode Materials: Application of the Hybrid Eigenvector-Following Density Functional Theory (DFT) Method to Layered $Li_{0.5}MnO_2$. *Chem. Mater.* **2015**, *27* (16), 5550−5561.
(75) Kim, J.; Middlemiss, D. S.; Chernova, N. A.; Zhu, B. Y. X.; Masquelier, C.; Grey, C. P. Linking Local Environments and Hyperfine Shifts: A Combined Experimental and Theoretical ^{31}P and ^{7}Li Solid-State NMR Study of Paramagnetic Fe(III) Phosphates. *J. Am. Chem. Soc.* **2010**, *132* (47), 16825−16840.
(76) Middlemiss, D. S.; Ilott, A. J.; Clément, R. J.; Strobridge, F. C.; Grey, C. P. Density Functional Theory-Based Bond Pathway Decompositions of Hyperfine Shifts: Equipping Solid-State NMR to Characterize Atomic Environments in Paramagnetic Materials. *Chem. Mater.* **2013**, *25* (9), 1723−1734.
(77) Zhang, Y.; Castets, A.; Carlier, D.; Ménétrier, M.; Boucher, F. Simulation of NMR Fermi Contact Shifts for Lithium Battery Materials: The Need for an Efficient Hybrid Functional Approach. *J. Phys. Chem. C* **2012**, *116* (33), 17393−17402.
(78) Van de Walle, C. G.; Blöchl, P. E. First-Principles Calculations of Hyperfine Parameters. *Phys. Rev. B: Condens. Matter Mater. Phys.* **1993**, *47* (8), 4244−4255.
(79) Cava, R. J.; Murphy, D. W.; Zahurak, S. M. Lithium Insertion in Wadsley-Roth Phases Based on Niobium Oxide. *J. Electrochem. Soc.* **1983**, *130* (12), 2345−2351.
(80) Lin, C.; Hu, L.; Cheng, C.; Sun, K.; Guo, X.; Shao, Q.; Li, J.; Wang, N.; Guo, Z. Nano-$TiNb_2O_7$/Carbon Nanotubes Composite Anode for Enhanced Lithium-Ion Storage. *Electrochim. Acta* **2018**, *260*, 65−72.
(81) Cheng, Q.; Liang, J.; Zhu, Y.; Si, L.; Guo, C.; Qian, Y. Bulk $Ti_2Nb_{10}O_{29}$ as Long-Life and High-Power Li-Ion Battery Anodes. *J. Mater. Chem. A* **2014**, *2* (41), 17258−17262.
(82) Xing, W.; Kalland, L.-E.; Li, Z.; Haugsrud, R.; Stevenson, J. Defects and Transport Properties in $TiNb_2O_7$. *J. Am. Ceram. Soc.* **2013**, *96* (12), 3775−3781.
(83) Cava, R. J.; Murphy, D. W.; Rietman, E. A.; Zahurak, S. M.; Barz, H. Lithium Insertion, Electrical Conductivity, and Chemical Substitution in Various Crystallographic Shear Structures. *Solid State Ionics* **1983**, *9−10*, 407−411.
(84) Park, M.; Zhang, X.; Chung, M.; Less, G. B.; Sastry, A. M. A Review of Conduction Phenomena in Li-Ion Batteries. *J. Power Sources* **2010**, *195* (24), 7904−7929.
(85) Dreele, R. B. V.; Cheetham, A. K. The Structures of Some Titanium-Niobium Oxides by Powder Neutron Diffraction. *Proc. R. Soc. London, Ser. A* **1974**, *338* (1614), 311−326.
(86) Perfler, L.; Kahlenberg, V.; Wikete, C.; Schmidmair, D.; Tribus, M.; Kaindl, R. Nanoindentation, High-Temperature Behavior, and Crystallographic/Spectroscopic Characterization of the High-Refractive-Index Materials $TiTa_2O_7$ and $TiNb_2O_7$. *Inorg. Chem.* **2015**, *54* (14), 6836−6848.
(87) Lu, X.; Jian, Z.; Fang, Z.; Gu, L.; Hu, Y.-S.; Chen, W.; Wang, Z.; Chen, L. Atomic-Scale Investigation on Lithium Storage Mechanism in $TiNb_2O_7$. *Energy Environ. Sci.* **2011**, *4* (8), 2638.
(88) Zhu, Y.; Wang, C. Galvanostatic Intermittent Titration Technique for Phase-Transformation Electrodes. *J. Phys. Chem. C* **2010**, *114* (6), 2830−2841.
(89) Maricq, M. M.; Waugh, J. S. NMR in Rotating Solids. *J. Chem. Phys.* **1979**, *70* (7), 3300−3316.
(90) Griffin, J. M.; Wimperis, S.; Berry, A. J.; Pickard, C. J.; Ashbrook, S. E. Solid-State ^{17}O NMR Spectroscopy of Hydrous Magnesium Silicates: Evidence for Proton Dynamics. *J. Phys. Chem. C* **2009**, *113* (1), 465−471.
(91) Griffin, J. M.; Miller, A. J.; Berry, A. J.; Wimperis, S.; Ashbrook, S. E. Dynamics on the Microsecond Timescale in Hydrous Silicates Studied by Solid-State ^{2}H NMR Spectroscopy. *Phys. Chem. Chem. Phys.* **2010**, *12* (12), 2989−2998.
(92) Chang, H. J.; Trease, N. M.; Ilott, A. J.; Zeng, D.; Du, L.-S.; Jerschow, A.; Grey, C. P. Investigating Li Microstructure Formation on Li Anodes for Lithium Batteries by in Situ $^{6}Li/^{7}Li$ NMR and SEM. *J. Phys. Chem. C* **2015**, *119* (29), 16443−16451.
(93) Catti, M.; Pinus, I.; Knight, K. Lithium Insertion Properties of $Li_xTiNb_2O_7$ Investigated by Neutron Diffraction and First-Principles Modelling. *J. Solid State Chem.* **2015**, *229*, 19−25.
(94) Björk, H.; Lidin, S.; Gustafsson, T.; Thomas, J. O. Superlattice Formation in the Lithiated Vanadium Oxide Phases $Li_{0.67}V_6O_{13}$ and LiV_6O_{13}. *Acta Crystallogr., Sect. B: Struct. Sci.* **2001**, *57* (6), 759−765.
(95) Arrouvel, C.; Parker, S. C.; Islam, M. S. Lithium Insertion and Transport in the TiO_2-B Anode Material: A Computational Study. *Chem. Mater.* **2009**, *21*, 4778−4783.
(96) Qian, D.; Xu, B.; Cho, H.-M.; Hatsukade, T.; Carroll, K. J.; Meng, Y. S. Lithium Lanthanum Titanium Oxides: A Fast Ionic Conductive Coating for Lithium-Ion Battery Cathodes. *Chem. Mater.* **2012**, *24* (14), 2744−2751.
(97) Bhattacharya, J.; Van der Ven, A. First-Principles Study of Competing Mechanisms of Nondilute Li Diffusion in Spinel Li_xTiS_2. *Phys. Rev. B: Condens. Matter Mater. Phys.* **2011**, *83* (14), 144302.
(98) Henkelman, G.; Arnaldsson, A.; Jónsson, H. A Fast and Robust Algorithm for Bader Decomposition of Charge Density. *Comput. Mater. Sci.* **2006**, *36* (3), 354−360.
(99) Tang, W.; Sanville, E.; Henkelman, G. A Grid-Based Bader Analysis Algorithm without Lattice Bias. *J. Phys.: Condens. Matter* **2009**, *21* (8), No. 084204.
(100) Lin, C.; Yu, S.; Wu, S.; Lin, S.; Zhu, Z.-Z.; Li, J.; Lu, L. $Ru_{0.01}Ti_{0.99}Nb_2O_7$ as an Intercalation-Type Anode Material with a Large Capacity and High Rate Performance for Lithium-Ion Batteries. *J. Mater. Chem. A* **2015**, *3* (16), 8627−8635.
(101) Inada, R.; Mori, T.; Kumasaka, R.; Ito, R.; Tojo, T.; Sakurai, Y. Characterization of Vacuum-Annealed $TiNb_2O_7$ as High Potential Anode Material for Lithium-Ion Battery. *Int. J. Appl. Ceram. Technol.* **2019**, *16*, 264−272.

DOI: 10.1021/jacs.9b06669
J. Am. Chem. Soc. 2019, 141, 16706−16725

(102) Lin, C.; Yu, S.; Zhao, H.; Wu, S.; Wang, G.; Yu, L.; Li, Y.; Zhu, Z.-Z.; Li, J.; Lin, S. Defective $Ti_2Nb_{10}O_{27.1}$: An Advanced Anode Material for Lithium-Ion Batteries. *Sci. Rep.* **2015**, *5*, 17836.
(103) Deng, S.; Luo, Z.; Liu, Y.; Lou, X.; Lin, C.; Yang, C.; Zhao, H.; Zheng, P.; Sun, Z.; Li, J.; Wang, N.; Wu, H. $Ti_2Nb_{10}O_{29-x}$ Mesoporous Microspheres as Promising Anode Materials for High-Performance Lithium-Ion Batteries. *J. Power Sources* **2017**, *362*, 250−257.
(104) Yang, C.; Yu, S.; Ma, Y.; Lin, C.; Xu, Z.; Zhao, H.; Wu, S.; Zheng, P.; Zhu, Z.-Z.; Li, J.; Wang, N. Cr^{3+} and Nb^{5+} Co-Doped $Ti_2Nb_{10}O_{29}$ Materials for High-Performance Lithium-Ion Storage. *J. Power Sources* **2017**, *360*, 470−479.
(105) Hu, L.; Lu, R.; Tang, L.; Xia, R.; Lin, C.; Luo, Z.; Chen, Y.; Li, J. $TiCr_{0.5}Nb_{10.5}O_{29}$/CNTs Nanocomposite as an Advanced Anode Material for High-Performance Li^+-Ion Storage. *J. Alloys Compd.* **2018**, *732*, 116−123.
(106) Yang, C.; Yu, S.; Lin, C.; Lv, F.; Wu, S.; Yang, Y.; Wang, W.; Zhu, Z.-Z.; Li, J.; Wang, N.; Guo, S. $Cr_{0.5}Nb_{24.5}O_{62}$ Nanowires with High Electronic Conductivity for High-Rate and Long-Life Lithium-Ion Storage. *ACS Nano* **2017**, *11* (4), 4217−4224.
(107) Cava, R. J.; Batlogg, B.; Krajewski, J. J.; Poulsen, H. F.; Gammel, P.; Peck, W. F., Jr.; Rupp, L. W., Jr. Electrical and Magnetic Properties of $Nb_2O_{5-\delta}$ Crystallographic Shear Structures. *Phys. Rev. B: Condens. Matter Mater. Phys.* **1991**, *44* (13), 6973−6981.
(108) Waldron, J. E. L.; Green, M. A.; Neumann, D. A. Charge and Spin Ordering in Monoclinic $Nb_{12}O_{29}$. *J. Am. Chem. Soc.* **2001**, *123* (24), 5833−5834.
(109) Andersen, E. N.; Klimczuk, T.; Miller, V. L.; Zandbergen, H. W.; Cava, R. J. Nanometer Structural Columns and Frustration of Magnetic Ordering in $Nb_{12}O_{29}$. *Phys. Rev. B: Condens. Matter Mater. Phys.* **2005**, *72* (3), No. 033413.
(110) Cava, R. J.; Batlogg, B.; Krajewski, J. J.; Gammel, P.; Poulsen, H. F.; Peck, W. F.; Rupp, L. W. Antiferromagnetism and Metallic Conductivity in $Nb_{12}O_{29}$. *Nature* **1991**, *350* (6319), 598−600.
(111) Rüscher, C. H. The Structural Effect on the Electrical Properties of $NbO_{2.5-x}$ Block-Type Compounds. *Phys. C* **1992**, *200* (1−2), 129−139.
(112) Morgan, B. J.; Scanlon, D. O.; Watson, G. W. Small Polarons in Nb- and Ta-Doped Rutile and Anatase TiO_2. *J. Mater. Chem.* **2009**, *19* (29), 5175.
(113) Du, L.-S.; Schurko, R. W.; Lim, K. H.; Grey, C. P. A Solid-State ^{93}Nb and ^{19}F NMR Spectroscopy and X-Ray Diffraction Study of Potassium Heptafluoroniobate(V): Characterization of ^{93}Nb, ^{19}F Coupling, and Fluorine Motion. *J. Phys. Chem. A* **2001**, *105* (4), 760−768.
(114) Michaelis, V. K.; Levin, K.; Germanov, Y.; Lelong, G.; Kroeker, S. Ultrahigh-Resolution ^7Li Magic-Angle Spinning Nuclear Magnetic Resonance Spectroscopy by Isotopic Dilution. *Chem. Mater.* **2018**, *30* (16), 5521−5526.
(115) Wi, S.; Frydman, L. Residual Dipolar Couplings between Quadrupolar Nuclei in High Resolution Solid State NMR: Description and Observations in the High-Field Limit. *J. Chem. Phys.* **2000**, *112* (7), 3248−3261.
(116) Jakobsen, H. J.; Bildsøe, H.; Brorson, M.; Gan, Z.; Hung, I. Direct Observation of $^{17}O-^{185/187}Re$ ^1J-Coupling in Perrhenates by Solid-State ^{17}O VT MAS NMR: Temperature and Self-Decoupling Effects. *J. Magn. Reson.* **2013**, *230*, 98−110.
(117) Islam, M. S.; Driscoll, D. J.; Fisher, C. A. J.; Slater, P. R. Atomic-Scale Investigation of Defects, Dopants, and Lithium Transport in the $LiFePO_4$ Olivine-Type Battery Material. *Chem. Mater.* **2005**, *17* (20), 5085−5092.
(118) Saritha, D.; Pralong, V.; Varadaraju, U. V.; Raveau, B. Electrochemical Li Insertion Studies on $WNb_{12}O_{33}$—A Shear ReO_3 Type Structure. *J. Solid State Chem.* **2010**, *183* (5), 988−993.
(119) Yan, L.; Lan, H.; Yu, H.; Qian, S.; Cheng, X.; Long, N.; Zhang, R.; Shui, M.; Shu, J. Electrospun $WNb_{12}O_{33}$ Nanowires: Superior Lithium Storage Capability and Their Working Mechanism. *J. Mater. Chem. A* **2017**, *5* (19), 8972−8980.
(120) Inada, R.; Kumasaka, R.; Inabe, S.; Tojo, T.; Sakurai, Y. Li^+ Insertion/Extraction Properties for $TiNb_2O_7$ Single Particle Characterized by a Particle-Current Collector Integrated Microelectrode. *J. Electrochem. Soc.* **2019**, *166* (3), A5157−A5162.

DOI: 10.1021/jacs.9b06669
J. Am. Chem. Soc. 2019, 141, 16706−16725